Mathematics

https://www.aimspress.com/journal/Math

AIMS Mathematics, 11(9): 29934–29977.
DOI: 10.3934/math.20261188
Received: 21 November 2025
Revised: 07 August 2026
Accepted: 21 August 2026
Published: 15 September 2026

Research article

Wavelet-enhanced adaptive meshing: Optimizing finite element simulations for structural and fluid dynamics

Mohamed Ayari[1], Zeineb Klai[2,*], Atef Gharbi[3], Omar Kahouli[4], Sulaiman A. Almohaimeed[5,*], Fahd Alhamazani[2] and Nasser Albalwi[2]

[1] Department of Information Technology, Faculty of Computing and Information Technology, Northern Border University, Kingdom of Saudi Arabia
[2] Department of Computer Sciences, Faculty of Computing and Information Technology, Northern Border University, Kingdom of Saudi Arabia
[3] Department of Information Systems, Faculty of Computing and Information Technology, Northern Border University, Kingdom of Saudi Arabia
[4] Department of Electronics Engineering, Applied College, University of Ha'il, Ha'il 2440, Saudi Arabia
[5] Department of Electrical Engineering, College of Engineering, Qassim University, Saudi Arabia

* **Correspondence:** Email: Zeineb.klai@nbu.edu.sa; Sulaiman.m@qu.edu.sa.

Abstract: This paper presents a practical integration of wavelet analysis with the finite element method (FEM) for adaptive mesh refinement in structural and fluid-dynamics simulations. At each adaptive cycle, the computed finite element solution is decomposed using a multiresolution wavelet transform, and the resulting detail coefficients are converted into element-level refinement indicators. Elements associated with the largest localized variations are refined, after which the finite element matrices and load vectors are reassembled on the updated mesh. The proposed procedure was evaluated using a simply supported vibrating beam and a two-dimensional flat-plate boundary-layer problem at $Re_L = 1000$. For the beam benchmark, the wavelet-adapted mesh uses 60 elements, compared with 160 elements for a uniformly refined mesh of similar modal accuracy, corresponding to an element-count reduction of approximately 62%. The modal-solution time decreases from 4.40 to 1.90 s. For the flat-plate problem, the adapted mesh uses 4096 elements instead of 16,384 elements and reduces the time required to reach the steady solution from 162 to 68 s. The adapted beam solution predicts the first three natural frequencies with a maximum relative error below 4%, while the flat-plate solution reproduces the end-of-plate skin-friction coefficient and integrated drag coefficient within approximately 4% and 2% of the corresponding laminar correlations, respectively. The results indicate that wavelet detail coefficients can provide useful localized refinement information when they are consistently coupled with element marking, mesh updating, and finite element reassembly. The computational overhead, parameter sensitivity, applicability, and limitations of the approach are also discussed.

Keywords: wavelet transform; adaptive mesh refinement; finite element method; structural dynamics; boundary-layer flow; multiresolution analysis; computational efficiency
Mathematics Subject Classification: 65N30, 65T60, 65M50, 76M10

1. Introduction

The finite element method (FEM) is one of the principal numerical techniques used to approximate partial differential equations arising in engineering and applied science. Its ability to represent complex geometries, heterogeneous materials, and different boundary conditions has made it an established tool in structural mechanics, vibration, acoustics, heat transfer, and fluid dynamics. Representative applications include the dynamic analysis of seismically excited structures [1], three-dimensional structural vibration [2], acoustic modal analysis [3], and room-acoustic simulation [4].

The accuracy and computational cost of a finite element solution depend strongly on the spatial discretization [5]. A coarse mesh may fail to represent localized phenomena such as large structural curvature, stress concentrations, crack evolution, thin boundary layers, steep velocity gradients, and singular solution behavior. Uniform refinement can improve the approximation, but it also introduces additional degrees of freedom in regions where the solution is already sufficiently smooth. This unnecessary refinement becomes particularly expensive in multidimensional, nonlinear, eigenvalue, and time-dependent problems, where the discrete system may need to be assembled and solved repeatedly.

Adaptive refinement has also been applied to large-scale three-dimensional structural topology optimization [6], thermomechanical crack propagation [7], phase-field fracture calculations based on recovery-type error estimates [8], and higher-order eigenvalue problems [9]. Recent studies have further demonstrated the value of localized refinement in complex structural and multiphysics calculations. Wang et al. developed an h-version adaptive finite element scheme for the free-vibration eigensolutions of three-dimensional cracked elastic bodies using an element subdivision–based error estimator [10], while Jambunathan et al. applied mesh refinement to relativistic magnetic-reconnection simulations and demonstrated substantial computational savings relative to a uniformly high-resolution grid [11].

Wavelet analysis provides a complementary mechanism for identifying localized behavior. A wavelet representation separates a field into approximation components, which describe its smooth or low-frequency behavior, and detail components, which reveal localized variations at different scales. In contrast to a global Fourier representation, a wavelet transform retains information about both the position and characteristic scale of a feature. The mathematical foundations and engineering applications of wavelet systems were presented comprehensively by Akujuobi [12], while the localization, efficiency, and application differences between Fourier and wavelet transforms were examined by Klai et al. [13].

The localization and multiresolution properties of wavelets have encouraged their integration with numerical discretization methods. Stevenson et al. [14] developed an adaptive method employing wavelets in time and finite elements in space for parabolic evolution equations. Kestler et al. [15] proposed an efficient space–time adaptive wavelet Galerkin method for time-periodic parabolic partial differential equations. Related developments in operator preconditioning and simultaneous space–time formulations were investigated by van Venetië [16], while van Venetië and Westerdiep [17] presented an efficient adaptive framework combining temporal wavelets with spatial finite elements.

Wavelet-based techniques have also been applied to spatially localized and multiscale problems. Fu et al. [18] developed a wavelet-based edge multiscale finite element method for singularly perturbed convection–diffusion equations, in which thin solution layers and small diffusion parameters require carefully localized resolution. Wei and Xiang [19] introduced a B-spline wavelet boundary element method for three-dimensional problems, demonstrating how wavelet bases can be used to organize complex numerical approximations.

In structural mechanics, Sun et al. [2] proposed a three-dimensional B-spline wavelet finite element method for vibration analysis. Their formulation used the approximation and localization properties of wavelet bases to represent structural modes efficiently. Sun et al. [3] subsequently applied a wavelet-based finite element approach to three-dimensional interior acoustic modeling and modal analysis. More recently, Ding et al. [20] developed a semi-analytical wavelet finite element method for wave propagation in rectangular rods. These studies demonstrate the continuing development of wavelet finite element formulations for vibration, modal, acoustic, and wave-propagation problems. Recent developments in plate and shell finite elements further emphasize that numerical performance depends not only on mesh resolution but also on the underlying element formulation, particularly in bending- and shear-dominated problems where shear locking, interpolation quality, and mesh sensitivity must be carefully controlled [21–24].

Wavelet-enhanced adaptivity has also been investigated in fracture and multiphysics applications. Dan et al. [25] combined wavelet enhancement with a cohesive-zone phase-field finite element model to study crack evolution in piezoelectric composites. More generally, phase-field research has emphasized the need for sufficiently fine and appropriately localized discretization around evolving fracture regions [26]. The recent adaptive studies cited above [7,8] further demonstrate the importance of controlling mesh resolution around strongly localized damage and crack zones. Classical recovery- and residual-based adaptive frameworks provide established alternatives for local error control [27,28], while recent phase-field fracture studies have demonstrated the effectiveness of adaptive and locally refined finite element strategies for resolving evolving crack regions efficiently [29,30].

For incompressible flow, Mishin et al. [31] developed a wavelet-based adaptive finite element method for Stokes problems. Their formulation is particularly relevant because it combines multiresolution-based adaptation with a mixed velocity–pressure finite element system. Wavelet techniques have also been incorporated into adaptive computational fluid dynamics methods. Mehta et al. [32], for example, reviewed developments in the adaptive wavelet-collocation method for complex internal and external flows. These studies demonstrate that wavelet information can guide spatial adaptation, while stability, conservation, and pressure–velocity compatibility remain properties of the underlying numerical formulation. Wavelet transforms have additionally been applied to image encryption [33], long-term time-series forecasting [34], local-feature learning for face-forgery detection [35], and pipeline-dent signal denoising [36]. These works are not concerned directly with adaptive finite element analysis, but they illustrate the broader ability of wavelet representations to isolate localized or multiscale information from complex numerical data.

Despite the progress made in wavelet-based numerical methods, the practical integration of wavelet analysis into a conventional finite element adaptive loop remains nontrivial. Standard discrete wavelet algorithms are generally formulated for regularly ordered samples, whereas finite element solutions may be defined on unstructured, nonuniform, or locally refined meshes. A reproducible implementation must therefore explain how the finite element field is transferred to a wavelet-compatible representation, how coefficients at different scales are associated with physical elements, how the resulting indicators are normalized, and how the mesh-dependent finite element operators are updated after refinement. A second issue concerns the interpretation of wavelet detail coefficients. Large coefficients identify localized variation at one or more analyzed scales, but they do not automatically constitute rigorous a posteriori estimates of the finite element error. Their magnitude may reflect a physical gradient, an under-resolved feature, a singularity, a numerical oscillation, interpolation to the sampling grid, or the boundary-extension procedure used by the transform. Accordingly, the present study treats wavelet coefficients as refinement indicators rather than as guaranteed upper or lower bounds for the discretization error.

The present work develops a wavelet-enhanced adaptive finite element procedure for structural and fluid-dynamics simulations. At each adaptive cycle, a selected finite element solution field is transferred to an ordered sampling representation and analyzed using a multiresolution wavelet transform. The resulting detail information is aggregated into element-level indicators. Elements associated with the strongest localized variations are marked for refinement, after which the mesh-dependent matrices and vectors are reassembled, and the problem is solved on the updated mesh.

The proposed procedure is assessed through two applications. The first is a simply supported Euler–Bernoulli beam subjected to dynamic excitation. Its analytical modal frequencies, derived from classical structural-dynamics theory [37], provide reference values for evaluating the modal accuracy of the adapted finite element model. The second application considers a two-dimensional incompressible flow over a flat plate at $Re_L = 1000$. This problem is used to investigate whether the wavelet indicator can direct refinement toward the developing laminar boundary layer while retaining a comparatively coarse mesh in the outer-flow region.

The purpose of the study is not to replace residual-, recovery-, or goal-oriented adaptive finite element procedures. Instead, it investigates whether wavelet detail information can provide a practical and reusable field-based mechanism for guiding local refinement in different physical applications. Residual and recovery estimators remain particularly important when mathematically justified error control, equilibrium information, or proven reliability and efficiency properties are required [5,8].

The principal contributions of this study are as follows:

1. A systematic procedure is formulated for coupling finite element solution fields with multiresolution wavelet analysis.
2. The transfer of the finite element field to an ordered sampling representation and the subsequent mapping of wavelet detail information back to physical elements are described explicitly.
3. A normalized element-level refinement indicator is introduced to reduce dependence on the units and amplitude of the analyzed physical field.
4. A complete adaptive cycle is defined, including finite element solution, field sampling, wavelet decomposition, coefficient aggregation, element marking, local refinement, solution transfer, and system reassembly.

5. The procedure is assessed through structural-dynamics and laminar-flow applications using modal frequencies, frequency-response behavior, skin-friction and drag coefficients, field differences, element counts, and computational time.
6. The practical limitations of the method are examined, including sensitivity to the wavelet family, decomposition level, sampling resolution, boundary treatment, marking strategy, mixed finite element spaces, and computational overhead.

The remainder of the paper is organized as follows: Section 2 presents the mathematical foundations of wavelet multiresolution analysis and the finite element formulations used for structural dynamics and incompressible flow. Section 3 describes the wavelet–FEM coupling, indicator construction, normalization, marking rule, mesh-refinement procedure, and adaptive algorithm. Section 4 presents the vibrating-beam and flat-plate applications. Section 5 discusses numerical accuracy, computational efficiency, parameter sensitivity, limitations, and the relationship between the proposed indicator and conventional adaptive approaches. Section 6 presents the conclusions and directions for future work.

2. Mathematical background

2.1. Wavelet multiresolution analysis

Wavelet analysis represents a function using basis functions that are localized in both position and scale. This property distinguishes wavelets from global Fourier basis functions and makes them suitable for detecting spatially concentrated features such as sharp gradients, singularities, boundary layers, and local oscillations [10,11].

2.1.1. Continuous wavelet transform

Let $f \in L^2(\mathbb{R})$, and let ψ denote an admissible mother wavelet. The continuous wavelet transform of f is defined as

$$W_\psi f(a,b) = \frac{1}{\sqrt{|a|}} \int_{-\infty}^{+\infty} f(t)\, \psi^* \left(\frac{t-b}{a}\right) dt,\ a \neq 0, \tag{1}$$

where a is the scale parameter, b is the translation parameter, and ψ^* denotes the complex conjugate of ψ.

Small values of $|a|$ correspond to fine-scale features, whereas large values represent broader variations in the analyzed field. The normalization factor $1/\sqrt{|a|}$ preserves the L^2-norm of the scaled wavelet functions. In the present work, only positive scales are considered.

2.1.2. Discrete wavelet representation

For numerical applications, the scale and translation parameters are discretized. A function may then be represented in terms of approximation and detail coefficients as

$$f(t)=\sum_k c_{J_0,k}\,\phi_{J_0,k}(t)+\sum_{j=J_0}^{J_{\max}-1}\sum_k d_{j,k}\,\psi_{j,k}(t), \tag{2}$$

where

$$\phi_{J_0,k}(t)=2^{J_0/2}\phi\,(2^{J_0}t-k), \tag{3}$$

and

$$\psi_{j,k}(t)=2^{j/2}\psi\left(2^{j}t-k\right). \tag{4}$$

Here, $\phi_{J_0,k}$ denotes a scaling function, $\psi_{j,k}$ denotes a wavelet function, $c_{J_0,k}$ is an approximation coefficient, and $d_{j,k}$ is a detail coefficient. The index J_0 denotes the coarsest retained resolution level, while $J_{\max}$ denotes the finest analyzed level.

The approximation coefficients describe the smooth or low-frequency component of the signal. The detail coefficients represent localized variations that are not captured at the corresponding coarser resolution.

2.1.3. Two-dimensional wavelet decomposition

For a two-dimensional field $f(x,y)$, each decomposition level produces horizontal, vertical, and diagonal detail coefficients, denoted respectively by

$$H_j(x,y), V_j(x,y), D_j^{\text{diag}}(x,y).$$

A combined detail magnitude at level j is defined as

$$\mathcal{D}_j(x,y)=\left[H_j(x,y)^2+V_j(x,y)^2+\left(D_j^{\text{diag}}(x,y)\right)^2\right]^{1/2}. \tag{5}$$

The notation $\mathcal{D}_j$ is used for the combined detail magnitude to distinguish it from the diagonal component D_j^{diag}.

When several decomposition levels are retained, the multilevel detail magnitude is defined by

$$\mathcal{D}(x,y)^2=\sum_{j=1}^{J}\lambda_j\ \mathcal{D}_j(x,y)^2, \tag{6}$$

where $\lambda_j\geq 0$ is a scale-dependent weighting parameter. Equal weighting is obtained by taking

$$\lambda_j=1,\ j=1,\dots,J.$$

Alternative weighting strategies may be used when finer or coarser scales must be emphasized.

2.1.4. Discrete and stationary wavelet transforms

The discrete wavelet transform (DWT) applies low-pass and high-pass filtering followed by downsampling. It is computationally efficient, but the number of coefficients decreases at successive decomposition levels. Consequently, the direct spatial association between the coefficients and the original finite element regions becomes less straightforward.

The stationary wavelet transform (SWT) omits the downsampling operation. The coefficient arrays, therefore, retain the dimensions of the sampled field, facilitating spatial localization and subsequent mapping to physical finite elements.

In this paper, the term DWT is used when downsampling is applied, whereas SWT is used when the coefficient arrays preserve the original sample-grid dimensions. The more general term multiresolution wavelet analysis is used when a statement applies to both formulations.

2.2. Finite element formulation for structural dynamics

Consider an elastic structural domain Ω_s with displacement vector $u(t)$. After spatial finite element discretization, the semi-discrete structural-dynamics equations are

$$M\ddot{u}(t) + C\dot{u}(t) + Ku(t) = F(t), \tag{7}$$

where M, C, and K are the global mass, damping, and stiffness matrices, respectively; $u(t)$ is the vector of nodal degrees of freedom; and $F(t)$ is the applied load vector.

The static finite element equation

$$Ku = F \tag{8}$$

is obtained from Eq (7) when inertia and damping effects are neglected.

For undamped free vibration,

$$M\ddot{u} + Ku = 0. \tag{9}$$

Assuming a harmonic response of the form

$$u(t) = \phi e^{i\omega t}$$

leads to the generalized eigenvalue problem

$$(K - \omega^2 M)\phi = 0, \tag{10}$$

or equivalently,

$$K\phi_n = \omega_n^2 M\phi_n, \tag{11}$$

where ω_n and ϕ_n are the n-th natural angular frequency and mode shape, respectively. The corresponding natural frequency in hertz is

$$f_n = \frac{\omega_n}{2\pi}. \tag{12}$$

Euler–Bernoulli beam equation

For the beam benchmark considered in Section 4, the transverse displacement $w(x, t)$ is governed by

$$\rho A\frac{\partial^2 w}{\partial t^2}+c\frac{\partial w}{\partial t}+EI\frac{\partial^4 w}{\partial x^4}=q(x,t),\ 0<x<L, \tag{13}$$

where E is Young's modulus, I is the second moment of area, ρ is the material density, A is the cross-sectional area, c is the distributed viscous damping coefficient per unit length, and $q(x,t)$ is the distributed transverse load.

For a simply supported beam, the transverse displacement satisfies

$$w(0,t)=0, w(L,t)=0, \tag{14}$$

while the bending moment vanishes at the supports:

$$EI\,\frac{\partial^2 w}{\partial x^2}(0,t)=0, EI\,\frac{\partial^2 w}{\partial x^2}(L,t)=0. \tag{15}$$

Let v be an admissible test function satisfying the homogeneous essential boundary conditions. Multiplying Eq (13) by v, integrating over the beam length, and integrating the fourth-order term by parts twice gives

$$\int_0^L \rho\, A\, \ddot{w}\, v\, dx+\int_0^L c\ \dot{w}\, v\, dx+\int_0^L E\, I\, w_{,xx}v_{,xx}\, dx=\int_0^L q\, v\, dx. \tag{16}$$

The natural boundary terms vanish under the simply supported moment conditions. Eq (16) forms the basis of the beam finite element discretization described in Section 4.

2.3. Finite element formulation for incompressible flow

Let $\Omega_f\subset\mathbb{R}^2$ denote the fluid domain. The velocity and pressure fields are written as

$$u=\begin{bmatrix}u\\ v\end{bmatrix},\ p.$$

The incompressible Navier–Stokes equations are

$$\rho\left[\frac{\partial u}{\partial t}+(u\cdot\nabla)u\right]-\nabla\cdot[2\mu\varepsilon(u)]+\nabla p=f\ \text{in}\ \Omega_f, \tag{17}$$

together with the incompressibility constraint

$$\nabla\cdot u=0\ \text{in}\ \Omega_f. \tag{18}$$

The strain-rate tensor is

$$\varepsilon(u)=\frac{1}{2}(\nabla u+\nabla u^T), \tag{19}$$

where ρ is the fluid density, μ is the dynamic viscosity, and f is the body-force vector.

The steady Navier–Stokes equations are obtained by setting

$$\frac{\partial u}{\partial t} = 0.$$

The Stokes equations are obtained by neglecting both the transient and convective terms. This distinction is maintained throughout the manuscript because the Stokes equations are a reduced form of the Navier–Stokes model rather than the general flow formulation.

2.3.1. Weak formulation

Let the boundary of the fluid domain be decomposed as

$$\partial\Omega_f = \Gamma_D \cup \Gamma_N,\ \Gamma_D \cap \Gamma_N = \emptyset.$$

For prescribed velocity data g on Γ_D, define the trial and test spaces as

$$V_g = \left\{u \in \left[H^1(\Omega_f)\right]^2 : u = g \text{ on } \Gamma_D\right\}, \tag{20}$$

$$V_0 = \left\{v \in \left[H^1(\Omega_f)\right]^2 : v = 0 \text{ on } \Gamma_D\right\}, \tag{21}$$

and

$$Q = L_0^2(\Omega_f) = \left\{q \in L^2(\Omega_f) : \int_{\Omega_f} q \ d\Omega = 0\right\}. \tag{22}$$

The weak problem is to find

$$(u, p) \in V_g \times Q$$

such that, for every

$$(v, q) \in V_0 \times Q,$$

$$\rho\left(\frac{\partial u}{\partial t}, v\right) + \rho\big((u \cdot \nabla), uv\big) + 2\mu\big(\varepsilon, (u)\varepsilon(v)\big) - (p, \nabla \cdot v) = (f, v) + \langle t_N, v\rangle_{\Gamma_N}, \tag{23}$$

and

$$(q, \nabla \cdot u) = 0. \tag{24}$$

Here, $(\cdot,\cdot)$ denotes the $L^2(\Omega_f)$ inner product, $\langle\cdot,\cdot\rangle_{\Gamma_N}$ denotes the boundary duality pairing, and t_N is the prescribed traction on Γ_N.

2.3.2. Discrete velocity–pressure spaces

Let

$$V_h \subset V_0,\ Q_h \subset Q$$

denote the finite-dimensional velocity test space and pressure space. A stable mixed finite element pair should satisfy the discrete inf–sup condition

$$\inf_{\substack{q_h \in Q_h \\ q_h \neq 0}} \sup_{\substack{v_h \in V_h \\ v_h \neq 0}} \frac{(q_h, \nabla \cdot v_h)}{\| q_h \|_{L^2(\Omega_f)} \ \| v_h \|_{H^1(\Omega_f)}} \geq \beta_0 > 0, \tag{25}$$

where β_0 is independent of the mesh size.

A commonly used example is the Taylor–Hood element pair, which employs quadratic interpolation for velocity and linear interpolation for pressure. If equal-order velocity and pressure interpolation is employed, an appropriate stabilization formulation is required. The exact velocity–pressure element pair used in the flat-plate calculation is specified in Section 4.2.

2.4. Wavelet coefficients as refinement indicators

The use of wavelet coefficients in adaptive refinement is motivated by their behavior in regions of different regularity. In smooth regions, detail coefficients generally decrease as the resolution level becomes finer. Near a sharp gradient, singularity, discontinuity, or under-resolved feature, comparatively large coefficients may persist across one or more scales.

This behavior motivates the construction of a local wavelet-based refinement indicator. For a one-dimensional field, an element indicator may be written as

$$\eta_e^2 = \sum_{\substack{j,k \\ \operatorname{supp}(\psi_{j,k}) \cap e \neq \emptyset}} \omega_{j,k,e} \left| d_{j,k} \right|^2, \tag{26}$$

where e is a finite element, $d_{j,k}$ is a wavelet detail coefficient, and $\omega_{j,k,e}$ is a nonnegative weight representing the association between the support of $\psi_{j,k}$ and element e.

For a sampled two-dimensional field, let

$$Q_e = \{(x_q, y_q) : (x_q, y_q) \in e\}$$

denote the set of wavelet-grid sampling points associated with element e. The element indicator may then be defined as

$$\eta_e = \left[\frac{1}{| Q_e |} \sum_{(x_q, y_q) \in Q_e} \mathcal{D}\left(x_q, y_q\right)^2 \right]^{1/2}, \tag{27}$$

where $| Q_e |$ is the number of sampling points associated with the element.

To reduce dependence on the physical units and amplitude of the analyzed field, the indicator is normalized as

$$\hat{\eta}_e = \frac{\eta_e}{\max\limits_{e' \in \mathcal{T}_h} \eta_{e'} + \epsilon_{\text{num}}}, \tag{28}$$

where $\mathcal{T}_h$ denotes the current finite element mesh, and $\epsilon_{\text{num}} > 0$ is a small numerical parameter introduced to avoid division by zero.

The normalized indicator satisfies

$$0 \leq \hat{\eta}_e \leq 1,$$

up to round-off error. Elements with the largest values of $\hat{\eta}_e$ are selected as candidates for refinement.

It is important to distinguish the proposed refinement indicator from a rigorous a posteriori error estimator. The wavelet indicator identifies localized multiscale content in the computed field, but it does not automatically satisfy the reliability and efficiency estimates of the form

$$C_{\mathrm{eff}}\eta \leq \| u - u_h \| \leq C_{\mathrm{rel}}\eta, \tag{29}$$

where C_{eff} and C_{rel} are mesh-independent constants.

Accordingly, the performance of the wavelet indicator is assessed in the present study through analytical modal frequencies, uniformly refined comparison solutions, engineering quantities such as skin friction and drag, field-level differences, and computational cost.

The preceding formulation establishes the mathematical basis of the structural and fluid finite element models and explains why wavelet detail coefficients may be used to identify regions of localized variation. Their practical integration into the finite element workflow requires a consistent procedure for field sampling, coefficient aggregation, element marking, mesh updating, solution transfer, and system reassembly. These operations are presented in Section 3.

3. Wavelet-enhanced adaptive finite element method

The proposed method augments a conventional finite element analysis with a multiresolution wavelet stage used to identify regions requiring additional spatial resolution. The governing finite element formulation is retained without modification. Wavelet detail coefficients are evaluated from the computed solution field, converted into element-level refinement indicators, and used to guide local mesh refinement.

At adaptive cycle m, the computational sequence is shown in Figure 1:

finite element solution $\Longrightarrow$ field sampling $\Longrightarrow$ wavelet decomposition $\Longrightarrow$ indicator construction $\Longrightarrow$ element marking $\Longrightarrow$ mesh refinement $\Longrightarrow$ system reassembly.

Figure 1. Wavelet-enhanced adaptive finite element procedure.

The computed finite element field is evaluated on an ordered sampling grid, decomposed through multiresolution wavelet analysis, and converted into element-level indicators. Elements with the largest normalized indicators are marked and refined before the finite element system is reassembled. The procedure is repeated for the prescribed number of adaptive cycles or until the selected convergence criterion is satisfied.

3.1. Finite element solution on the current mesh

Let $\mathcal{T}_h^{(m)}$ denote the finite element mesh at adaptive cycle m, and let $V_h^{(m)}$ be the corresponding finite element space. The numerical solution is denoted by $u_h^{(m)} \in V_h^{(m)}$.

The discrete problem is written in the general form

$$\mathcal{A}^{(m)}\left(u_h^{(m)}, v_h\right) = \mathcal{F}^{(m)}(v_h),\ \forall v_h \in V_h^{(m)}, \tag{30}$$

where $\mathcal{A}^{(m)}$ represents the mesh-dependent finite element operator, and $\mathcal{F}^{(m)}$ denotes the corresponding loading functional.

For the structural problem, the semi-discrete equation is

$$M^{(m)}\ddot{u}^{(m)} + C^{(m)}\dot{u}^{(m)} + K^{(m)}u^{(m)} = F^{(m)}(t). \tag{31}$$

For the fluid problem, Equation (30) represents the discrete mixed velocity–pressure formulation introduced in Section 2.

3.2. Selection of the analyzed field

The field supplied to the wavelet transform is selected according to the physical feature to be resolved.

For the beam benchmark, the analyzed quantity is the transverse displacement field:

$$g_h^{(m)}(x) = w_h^{(m)}(x). \tag{32}$$

For the flat-plate benchmark, the analyzed quantity is the streamwise velocity component:

$$g_h^{(m)}(x,y) = u_h^{(m)}(x,y). \tag{33}$$

The streamwise velocity is used because the developing boundary layer is characterized by a strong wall-normal variation in this component. The use of the same field throughout all adaptive cycles ensures that changes in the indicator distribution result from the evolving solution and mesh rather than from a change in the analyzed physical quantity.

3.3. Transfer to a wavelet-compatible sampling grid

The finite element solution is generally defined on a nonuniform mesh, whereas conventional discrete and stationary wavelet transforms require ordered samples. The computed finite element field is, therefore, evaluated at a set of regularly distributed sampling points

$$\mathcal{G} = \{x_q\}_{q=1}^{N_G}, \tag{34}$$

where N_G is the total number of sampling locations.

The transfer from the finite element space to the sampling representation is denoted by $\Pi_G\colon V_h^{(m)} \to G_h$.

The sampled field is

$$g_G^{(m)}(x_q) = \Pi_G g_h^{(m)}(x_q). \tag{35}$$

If the sampling point x_q lies in element e_q, finite element interpolation gives

$$g_G^{(m)}(x_q) = \sum_{i\in\mathcal{N}(e_q)} N_i\,(x_q) g_i^{(m)}, \tag{36}$$

where $\mathcal{N}(e_q)$ is the set of nodes of element e_q, N_i is the corresponding finite element shape function, and $g_i^{(m)}$ is the nodal value of the analyzed field.

For the beam problem, the field is sampled along the beam axis. For the flat-plate problem, it is evaluated on a Cartesian grid covering the computational domain. This transfer is used only for wavelet analysis and does not modify the finite element solution or mesh.

The sampling spacing Δ_G is selected relative to the minimum element size according to

$$\Delta_G \leq \kappa h_{\min}^{(m)}, \tag{37}$$

where $h_{\min}^{(m)}$ is the smallest element dimension at cycle m, and κ is the sampling factor. The sampling spacing is selected relative to the minimum element size according to Eq (37), thereby ensuring that the wavelet-analysis grid remains sufficiently fine to represent the spatial variations resolved by the current finite element mesh.

3.4. Wavelet decomposition

The sampled one-dimensional beam field is analyzed using a discrete wavelet transform. The decomposition produces approximation and detail coefficients:

$$g_G^{(m)} \longrightarrow \left\{c_{J,k}^{(m)}, d_{j,k}^{(m)}\right\}. \tag{38}$$

For the two-dimensional flat-plate field, a stationary wavelet transform is used so that the coefficient arrays retain the dimensions of the sampling grid. At each level j, the transform produces horizontal, vertical, and diagonal detail coefficients:

$$H_j^{(m)}(x,y),\ V_j^{(m)}(x,y),\ D_{j,\mathrm{diag}}^{(m)}(x,y).$$

The combined detail magnitude at level j is defined as

$$\mathcal{D}_j^{(m)}(x,y) = \left[\left(H_j^{(m)}(x,y)\right)^2 + \left(V_j^{(m)}(x,y)\right)^2 + \left(D_{j,\mathrm{diag}}^{(m)}(x,y)\right)^2\right]^{1/2}. \tag{39}$$

When several decomposition levels are retained, the multilevel detail magnitude is

$$\left(\mathcal{D}^{(m)}(x,y)\right)^2 = \sum_{j=1}^{J} \lambda_j \left(\mathcal{D}_j^{(m)}(x,y)\right)^2, \tag{40}$$

where J is the number of decomposition levels, and λ_j is the weight associated with level j. Equal weighting is used in the present work:

$$\lambda_j = 1,\ j = 1, \dots, J. \tag{41}$$

Both benchmarks use the Daubechies-4 wavelet with two decomposition levels. A one-dimensional DWT is used for the beam, whereas a two-dimensional SWT is used for the flat-plate field.

3.5. Element-level refinement indicator

Wavelet coefficients are defined on the sampling representation, whereas the refinement operation is applied to physical finite elements. The wavelet information is therefore aggregated over the sampling points associated with each element.

For $e \in \mathcal{T}_h^{(m)}$, let

$$Q_e = \{x_q \in \mathcal{G}: x_q \in e\} \tag{42}$$

be the set of sampling points contained in element e.

For the two-dimensional field, the element indicator is defined by the root-mean-square detail magnitude:

$$\eta_e^{(m)} = \left[\frac{1}{|Q_e|}\sum_{x_q \in Q_e}\left(\mathcal{D}^{(m)}(x_q)\right)^2\right]^{1/2}, \tag{43}$$

where $|Q_e|$ is the number of sampling points associated with element e.

For the one-dimensional DWT, the corresponding support-based indicator is

$$\left(\eta_e^{(m)}\right)^2 = \sum_{\substack{j,k \\ \operatorname{supp}(\psi_{j,k}) \cap e \neq \emptyset}} \omega_{j,k,e}\left|d_{j,k}^{(m)}\right|^2, \tag{44}$$

where $\omega_{j,k,e}$ represents the fraction of the wavelet support associated with element e.

Equations (43) and (44) convert wavelet detail information into a scalar value assigned to each finite element. Large values identify elements associated with strong localized variation in the analyzed field.

The successive stages of the coefficient-to-element mapping procedure are illustrated in Figure 2, beginning with the sampled finite element field and ending with the set of elements selected for refinement.

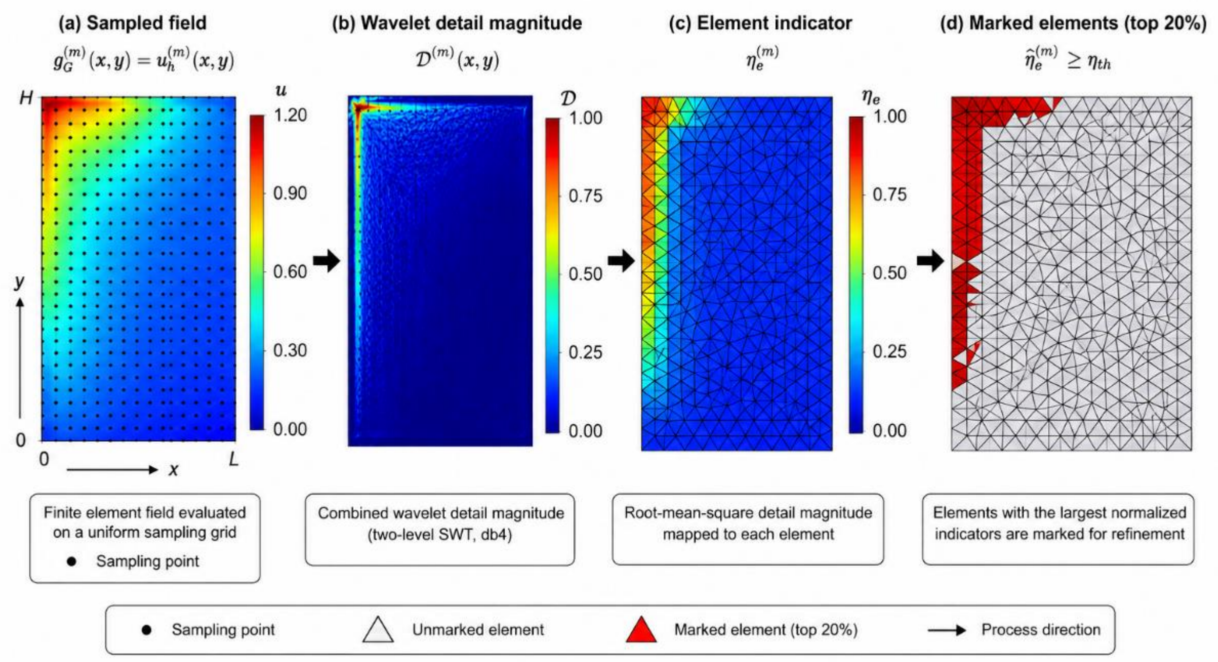

Figure 2. Mapping of wavelet detail information to the finite element mesh.

The finite element field is first evaluated on an ordered sampling grid and then decomposed using a two-level stationary wavelet transform with the Daubechies-4 wavelet. The multilevel detail magnitude is aggregated over the sampling points associated with each element to construct the element-level indicator. The elements corresponding to the highest 20% of the normalized indicator values are marked for refinement.

3.6. Indicator normalization

The magnitude of a wavelet coefficient depends on the units and amplitude of the analyzed field, the selected wavelet, and the decomposition level. The element indicators are therefore normalized at each adaptive cycle:

$$\hat{\eta}_e^{(m)} = \frac{\eta_e^{(m)}}{\max\limits_{e' \in \mathcal{T}_h^{(m)}} \eta_{e'}^{(m)} + \epsilon_{\text{num}}}, \tag{45}$$

where $\epsilon_{\text{num}} > 0$ is a small numerical constant introduced to avoid division by zero.

The normalized indicator satisfies

$$0 \le \hat{\eta}_e^{(m)} \le 1. \tag{46}$$

This normalization permits the same marking procedure to be applied to the structural displacement and fluid velocity fields without comparing their dimensional coefficient values directly.

3.7. Element marking

The elements are ranked in descending order according to their normalized indicators. At each adaptive cycle, the highest $p\%$ of the elements are selected:

$$\mathcal{M}^{(m)} = \text{TopFraction}\left(\left\{\hat{\eta}_e^{(m)}\right\}_{e \in \mathcal{T}_h^{(m)}}, p\right), \tag{47}$$

where $\mathcal{M}^{(m)}$ denotes the marked-element set.

The present calculations use

$$p = 20\%. \tag{48}$$

Fixed-fraction marking avoids the use of a common dimensional threshold for displacement and velocity. The number of elements created after refinement may exceed the number selected directly by Eq (47), because additional neighboring elements can be subdivided to maintain mesh conformity.

3.8. Mesh refinement and conformity

Marked beam elements are subdivided by bisection. In the two-dimensional mesh, each marked element is subdivided according to the refinement rule associated with its element type. Neighboring elements are subsequently checked, and additional subdivisions are introduced where necessary to preserve conformity and limit abrupt changes in element size.

The refined mesh is denoted by

$$\mathcal{T}_h^{(m+1)}. \tag{49}$$

The resulting mesh therefore contains elements marked directly by the wavelet indicator together with any additional elements required by the conformity procedure.

3.9. Solution transfer

After refinement, the solution from the previous mesh is transferred to the new finite element space: $\mathcal{P}^{(m\to m+1)}: V_h^{(m)} \to V_h^{(m+1)}$.

The transferred solution is

$$u_{h,0}^{(m+1)} = \mathcal{P}^{(m\to m+1)} u_h^{(m)}. \tag{50}$$

Nodal interpolation is used to initialize the solution on the refined mesh. For structural dynamics, the displacement and velocity vectors are transferred. For the fluid problem, the velocity and pressure fields are transferred and subsequently corrected through the renewed nonlinear finite element solution.

3.10. Reassembly and solution on the refined mesh

Mesh refinement changes the finite element basis functions and all mesh-dependent operators. The structural mass, damping, stiffness, and load terms are therefore reassembled on the new mesh:

$$M^{(m+1)},\ C^{(m+1)},\ K^{(m+1)},\ F^{(m+1)}.$$

For the flow problem, the diffusion, convection, pressure-coupling, and continuity operators are reconstructed.

The updated problem is then solved:

$$\mathcal{A}^{(m+1)}\left(u_h^{(m+1)}, v_h\right) = \mathcal{F}^{(m+1)}(v_h), \forall v_h \in V_h^{(m+1)}. \tag{51}$$

The wavelet stage therefore influences only the spatial distribution of the mesh. The governing structural and fluid equations remain those defined by the finite element formulations in Section 2.

3.11. Stopping criteria

The adaptive procedure is terminated when the prescribed number of adaptive cycles is reached or when the monitored quantity of interest changes by less than a specified tolerance.

For a quantity of interest $J(u_h)$, the relative change between two successive cycles is

$$\varepsilon_J^{(m+1)} = \frac{\left|J\left(u_h^{(m+1)}\right) - J\left(u_h^{(m)}\right)\right|}{\left|J\left(u_h^{(m+1)}\right)\right| + \epsilon_{\text{num}}}. \tag{52}$$

Convergence is assumed when

$$\varepsilon_J^{(m+1)} \le \varepsilon_{\mathrm{tol}}. \tag{53}$$

For the structural benchmark, the monitored quantities are the natural frequencies and resonance locations. For the fluid benchmark, the monitored quantities are the skin-friction and drag coefficients. In the reported calculations, three adaptive cycles are applied, after which the monitored outputs satisfy the selected engineering-accuracy ranges.

3.12. Adaptive algorithm

Algorithm 1. Wavelet-enhanced adaptive finite element procedure

Input: Initial mesh $\mathcal{T}_h^{(0)}$, finite element model, analyzed solution field, wavelet family, decomposition level J, marking fraction p, maximum number of adaptive cycles $M_{\max}$, and convergence tolerance $\varepsilon_{\mathrm{tol}}$.

1. Set $m = 0$.
2. Generate the initial finite element mesh and function space.
3. Assemble the finite element system.
4. Solve the finite element problem to obtain $u_h^{(m)}$.
5. Select the analyzed field $g_h^{(m)}$.
6. Evaluate $g_h^{(m)}$ on the ordered sampling grid.
7. Apply the DWT or SWT.
8. Compute the multilevel detail magnitude.
9. Aggregate the wavelet details into element indicators $\eta_e^{(m)}$.
10. Normalize the indicators to obtain $\hat{\eta}_e^{(m)}$.
11. Evaluate the stopping criterion.
12. If the stopping criterion is satisfied or $m = M_{\max}$, terminate.
13. Rank the elements and mark the highest $p\%$.
14. Refine the marked elements and enforce mesh conformity.
15. Transfer the previous solution to the refined finite element space.
16. Reassemble the mesh-dependent finite element system.
17. Set $m \leftarrow m + 1$ and return to Step 4.

Output: Adapted mesh, finite element solution, element-indicator distribution, and adaptive convergence history.

The complete computational sequence of Algorithm 1 is summarized graphically in Figure 3, which shows the iterative transition from the finite element solution to wavelet analysis, element marking, mesh refinement, reassembly, and convergence assessment.

The finite element problem is solved on the current mesh, the selected solution field is sampled and analyzed by wavelet decomposition, and the resulting detail information is mapped to element-level indicators. If the convergence criterion is not satisfied, the marked elements are refined, the solution is transferred, and the finite element system is reassembled before the next adaptive cycle. The principal wavelet and adaptive parameters used in the two numerical benchmarks are summarized in Table 1.

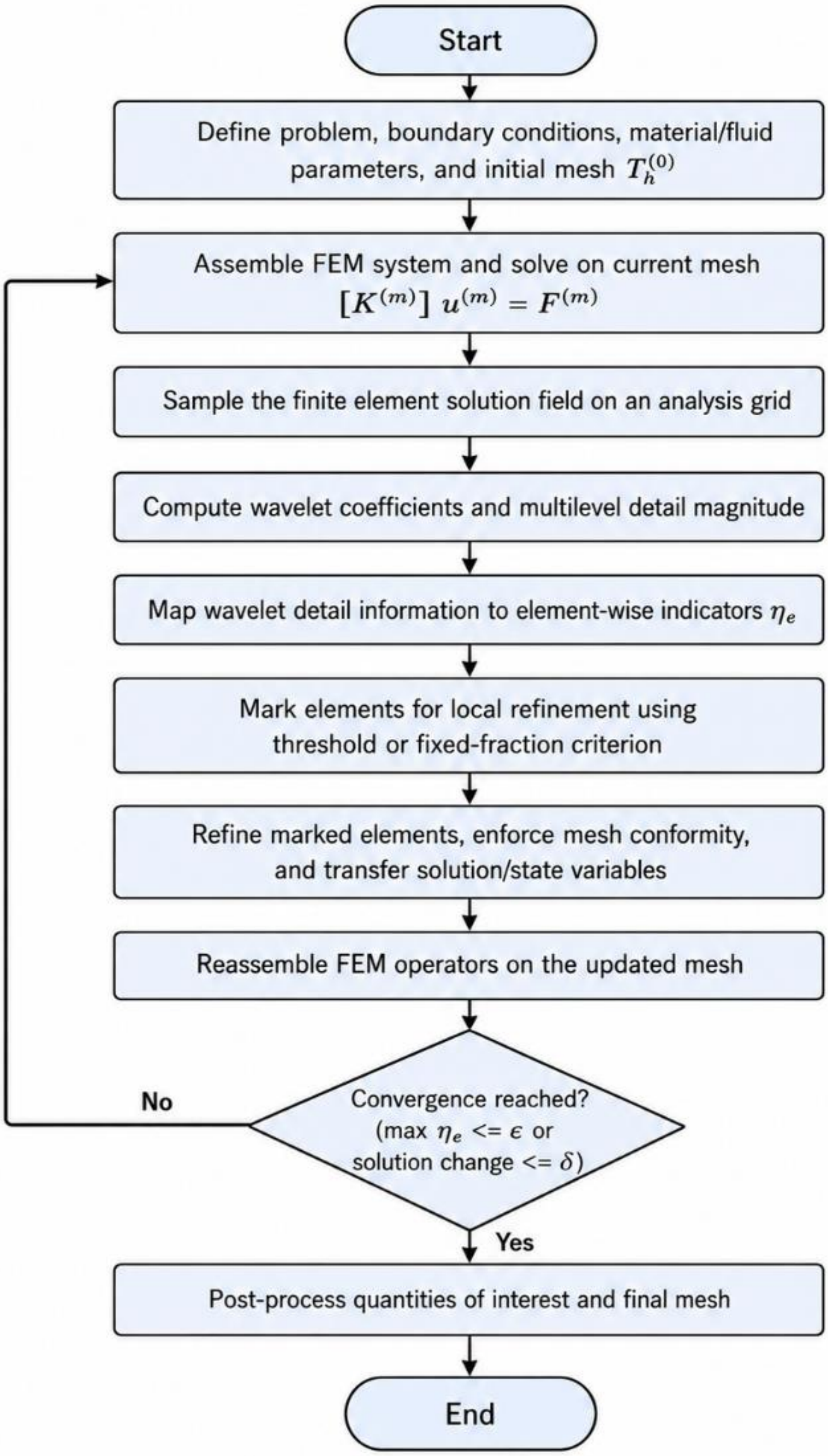

Figure 3. Flowchart of the wavelet-enhanced adaptive finite element algorithm.

The same adaptive framework is applied to both benchmarks, while the analyzed field and transform dimensionality are selected according to the physical problem. The numerical implementation and benchmark-specific settings are described in Section 4.

Table 1. Wavelet analysis and adaptive refinement parameters used for the beam and flat-plate benchmarks.

Parameter	Beam benchmark	Flat-plate benchmark
Analyzed field	Transverse displacement	Streamwise velocity
Transform	One-dimensional DWT	Two-dimensional SWT
Wavelet family	db4	db4
Decomposition levels	2	2
Level weighting	Equal	Equal
Marking strategy	Highest 20%	Highest 20%
Number of adaptive cycles	3	3
Solution transfer	Nodal interpolation	Nodal interpolation followed by renewed flow solution
Mesh conformity	Enforced	Enforced

3.13. Computational cost

The additional computational operations introduced by the method are field sampling, wavelet transformation, coefficient-to-element mapping, element marking, mesh refinement, and solution transfer.

Let N_G be the number of sampling points, N_{el} the number of finite elements, and J the number of wavelet levels. For a compactly supported DWT, the transform cost is approximately

$$T_{\mathrm{DWT}} = \mathcal{O}(N_G). \tag{54}$$

For a J-level SWT, the corresponding cost is

$$T_{\mathrm{SWT}} = \mathcal{O}(JN_G), \tag{55}$$

because the coefficient arrays are not downsampled.

The element-mapping operation has approximate complexity

$$T_{\mathrm{map}} = \mathcal{O}(N_G + N_{\mathrm{el}}). \tag{56}$$

For large finite element systems, assembly and algebraic solution generally remain the dominant computational costs. For smaller problems, the relative contribution of field transfer, wavelet analysis, and mesh reconstruction may be more noticeable. The contribution of these components to the total adaptive cost is discussed in Section 5.

4. Numerical applications and validation

The proposed wavelet-enhanced adaptive finite element procedure is evaluated using two applications with different physical characteristics. The first problem concerns the vibration of a simply supported Euler–Bernoulli beam and permits direct comparison with analytical natural frequencies. The second problem considers two-dimensional laminar flow over a flat plate at $Re_L = 1000$, for which the numerical wall-shear and drag quantities are compared with classical boundary-layer correlations.

In both applications, the adaptive process begins from a relatively coarse mesh. The selected finite element field is transferred to the sampling grid, analyzed using the wavelet parameters listed in Table 1, and mapped to element-level indicators. The highest 20% of the normalized indicators are marked during each adaptive cycle.

4.1. Simply supported beam

4.1.1. Physical model and material properties

A uniform Euler–Bernoulli beam of length L, rectangular width b, and height h is considered. The beam is simply supported at both ends and subjected to harmonic transverse excitation near its midpoint. The geometric and material properties are summarized in Table 2.

Table 2. Geometric, material, and numerical parameters of the beam benchmark.

Parameter	Symbol	Value
Beam length	L	1.00 m
Width	b	0.050 m
Height	h	0.010 m
Young's modulus	E	210 GPa
Density	ρ	7800 kg m^{-3}
Cross-sectional area	$A = bh$	5.0×10^{-4} m^2
Second moment of area	$I = bh^3/12$	4.167×10^{-9} m^4
Initial number of elements	$N_{\mathrm{el},0}$	12
Final adapted elements	$N_{\mathrm{el},a}$	60
Uniform-fine elements	$N_{\mathrm{el},u}$	160
Wavelet family	—	db4
Decomposition levels	J	2
Marking fraction	p	20%
Adaptive cycles	—	3

The beam geometry, support conditions, coordinate system, and location of the harmonic transverse excitation are shown in Figure 4.

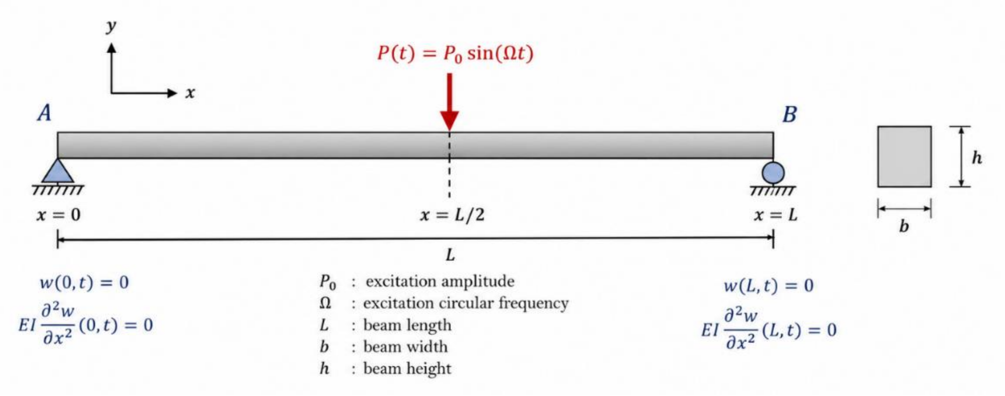

Figure 4. Geometry, supports, coordinate system, and harmonic transverse excitation of the simply supported beam.

The transverse-displacement and zero-moment boundary conditions are

$$w(0,t) = w(L,t) = 0, \tag{57}$$

and

$$EI\, w_{,xx}(0,t) = EI\, w_{,xx}(L,t) = 0. \tag{58}$$

For free vibration, the analytical mode shapes are

$$\phi_n(x) = \sin\left(\frac{n\pi x}{L}\right), \tag{59}$$

and the corresponding natural angular frequencies are

$$\omega_n = \left(\frac{n\pi}{L}\right)^2 \sqrt{\frac{EI}{\rho A}}. \tag{60}$$

The natural frequencies in hertz are, therefore,

$$f_n = \frac{1}{2\pi}\left(\frac{n\pi}{L}\right)^2 \sqrt{\frac{EI}{\rho A}}. \tag{61}$$

Using the parameters in Table 2 gives

$$f_1^{\text{exact}} = 23.53 \text{ Hz},\ f_2^{\text{exact}} = 94.11 \text{ Hz},\ f_3^{\text{exact}} = 211.76 \text{ Hz}. \tag{62}$$

These values are used as analytical references for evaluating the finite element solutions [27].

4.1.2. Finite element discretization

The beam is discretized using two-node Euler–Bernoulli elements with cubic Hermite interpolation. Each node has one transverse-displacement degree of freedom and one rotational degree of freedom. For N_{el} elements, the number of active degrees of freedom after applying the two displacement constraints is

$$N_{\text{dof}} = 2N_{\text{el}}. \tag{63}$$

Accordingly, the initial, adapted, and uniform-fine models contain 24, 120, and 320 active degrees of freedom, respectively.

The consistent element mass matrix and bending-stiffness matrix are assembled using the formulation described in Section 2. The undamped modal problem is written as

$$K\phi_n = \omega_n^2 M\phi_n. \tag{64}$$

For the harmonic response, the frequency-domain system is

$$[K - \Omega^2 M + i\Omega C]\hat{u}(\Omega) = \hat{F}(\Omega), \tag{65}$$

where Ω is the excitation angular frequency.

The midpoint frequency-response function is defined by

$$H_{\text{mid}}(\Omega) = \frac{\widehat{w}(L,/2\Omega)}{\hat{P}(\Omega)}. \tag{66}$$

4.1.3. Wavelet-guided adaptation

The computed transverse-displacement field is sampled along the beam axis and analyzed using a two-level db4 DWT. The wavelet details are associated with the beam elements using the support-based indicator defined by Eq (44).

The normalized indicator distribution on the initial mesh identifies the regions containing the strongest localized variations. The marked elements and any neighboring elements required by the mesh-refinement procedure are subdivided before the finite element matrices are reassembled.

The successive element counts obtained during the adaptive process are listed in Table 3.

Table 3. Beam mesh evolution during the adaptive procedure.

Adaptive cycle	Elements	Active degrees of freedom
0	12	24
1	28	56
2	44	88
3	60	120
Uniform-fine comparison	160	320

The increase in element count includes both elements marked directly by the wavelet indicator and additional subdivisions introduced by the refinement procedure.

Figure 5 compares the sampled transverse-displacement field on the initial beam mesh with the corresponding two-level db4 wavelet-detail magnitude used to construct the local refinement indicator.

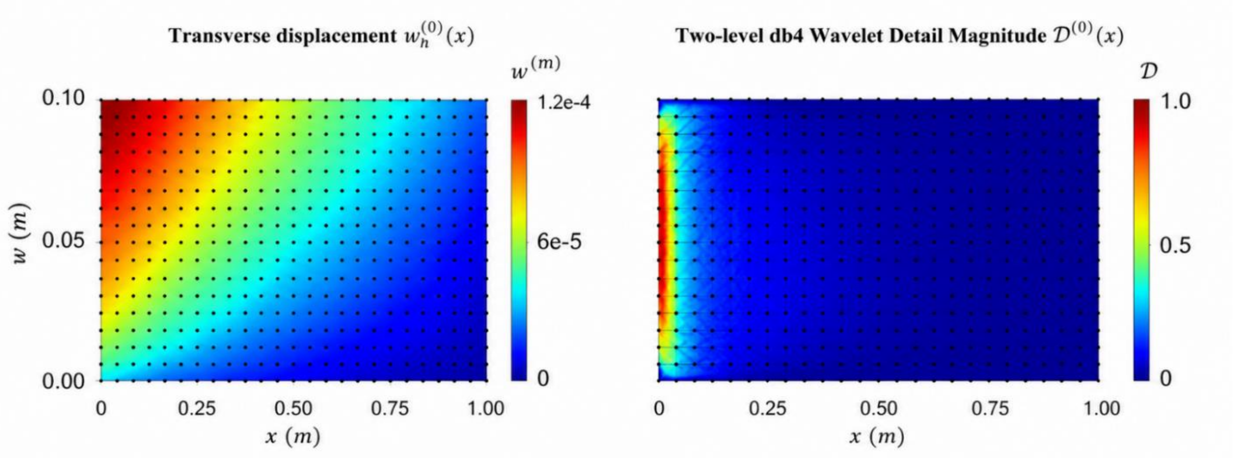

Figure 5. Transverse-displacement field and corresponding two-level db4 wavelet-detail magnitude on the initial beam mesh. Large detail coefficients contribute to the local element indicator used for refinement.

The redistribution of spatial resolution produced by the adaptive procedure is illustrated in Figure 6 through a direct comparison of the initial uniform mesh and the final wavelet-adapted mesh.

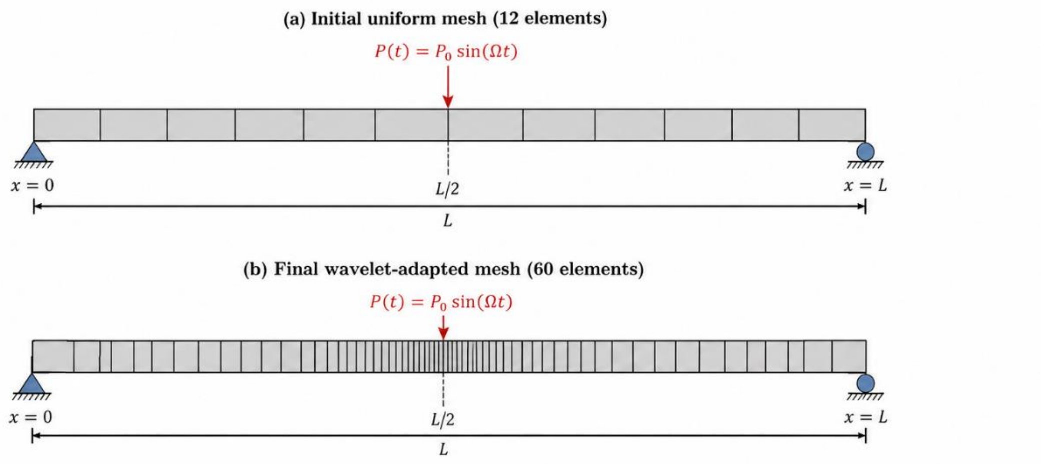

Figure 6. Initial uniform and final wavelet-adapted beam meshes. Element boundaries are shown explicitly, and the excitation position is indicated by the vertical dashed line.

4.1.4. Modal results

The relative error in the n-th natural frequency is calculated as

$$e_{f_n} = 100\frac{|f_{n,h} - f_n^{\text{exact}}|}{f_n^{\text{exact}}}. \tag{67}$$

The first three modal frequencies obtained using the initial, adapted, and uniform-fine meshes are reported in Table 4.

Table 4. Natural frequencies, relative errors, degrees of freedom, and modal-solution times.

Mesh	**Elements**	**Active DOFs**	f_1**(Hz)**	**Error (%)**	f_2**(Hz)**	**Error (%)**	f_3**(Hz)**	**Error (%)**	**Time (s)**
Initial uniform	12	24	21.80	7.3	80.10	14.9	152.30	28.1	0.60
Wavelet adapted	60	120	23.25	1.2	91.75	2.5	203.70	3.8	1.90
Uniform fine	160	320	23.29	1.0	92.04	2.2	204.30	3.5	4.40
Analytical	—	—	23.53	—	94.11	—	211.76	—	—

The initial mesh provides a reasonable approximation of the first mode but becomes progressively less accurate for the higher modes. The third-mode error reaches 28.1%, indicating that the coarse model does not provide adequate spatial resolution for higher modal curvature.

After three adaptive cycles, the frequency errors decrease to 1.2%, 2.5%, and 3.8%. The uniformly refined model gives slightly smaller errors of 1.0%, 2.2%, and 3.5%. Both the adapted and uniform-fine meshes, therefore, satisfy a maximum modal-error criterion of approximately 4%.

The adapted mesh uses 120 active degrees of freedom instead of 320. The reduction in active problem size is

$$R_{\mathrm{dof}} = 100\left(1 - \frac{120}{320}\right) = 62.5\%. \tag{68}$$

The reported modal-solution time decreases from 4.40 to 1.90 s:

$$R_{t,\mathrm{beam}} = 100\left(1 - \frac{1.90}{4.40}\right) = 56.8\%. \tag{69}$$

The corresponding runtime ratio is

$$S_{\mathrm{beam}} = \frac{4.40}{1.90} = 2.32. \tag{70}$$

Figure 7 compares the relative errors in the first three natural frequencies obtained using the initial, wavelet-adapted, and uniform-fine beam meshes.

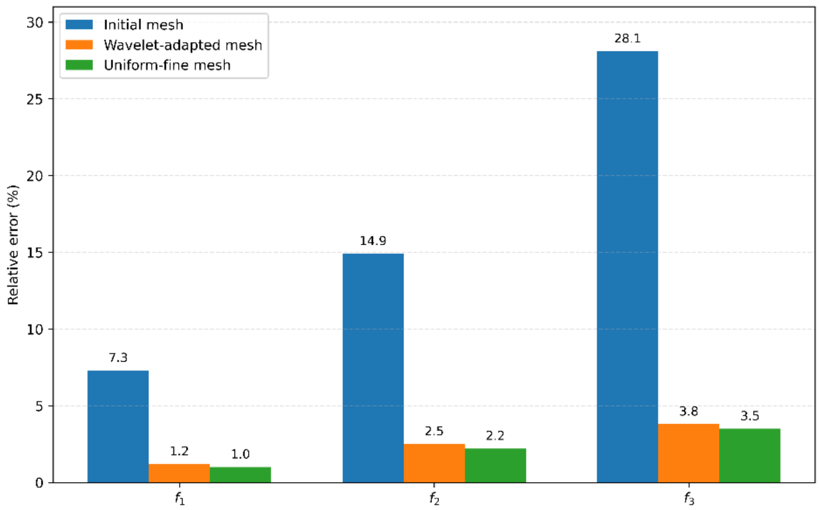

Figure 7. Relative errors in the first three natural frequencies for the initial, wavelet-adapted, and uniform-fine beam meshes.

4.1.5. Frequency-response results

The frequency-response calculation provides an additional assessment of the dynamic model. The adapted solution predicts the first two principal resonance locations at approximately

$$f_{r,1} = 23.4 \text{ Hz}, \; f_{r,2} = 93.1 \text{ Hz}. \tag{71}$$

Relative to the analytical frequencies, the deviations are approximately

$$e_{r,1} = 100\frac{|\,23.4 - 23.53\,|}{23.53} = 0.55\%, \tag{72}$$

and

$$e_{r,2} = 100 \frac{|\ 93.1 - 94.11\ |}{94.11} = 1.07\%. \tag{73}$$

These resonance locations are consistent with the eigenvalue results. The comparison focuses on resonance frequency rather than peak amplitude because the latter also depends on the damping model, excitation amplitude, and frequency discretization.

Figure 8 compares the midpoint frequency-response magnitudes obtained from the initial and wavelet-adapted beam meshes and shows their agreement with the first two analytical resonance frequencies.

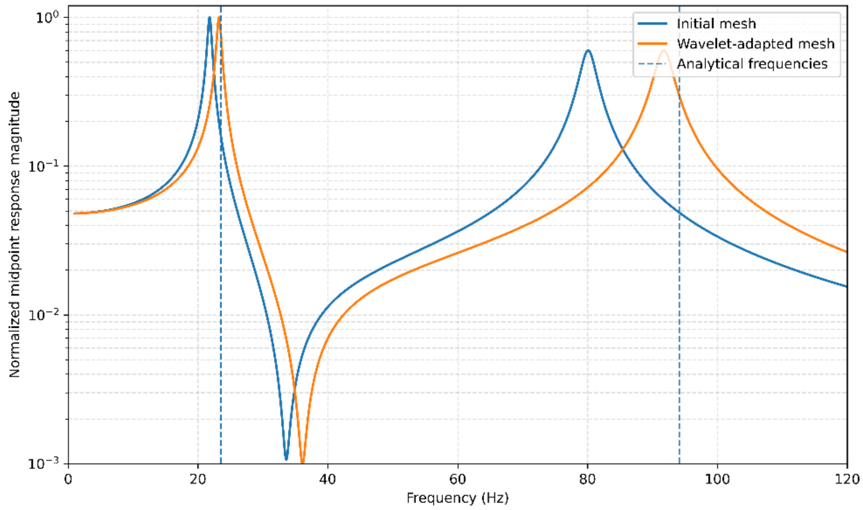

Figure 8. Reconstructed normalized midpoint frequency-response curves for the initial and wavelet-adapted beam models. The first two adapted resonance locations deviate from the corresponding analytical frequencies by approximately 0.55% and 1.07%, respectively.

4.2. Laminar flow over a flat plate

4.2.1. Problem definition

The second application considers two-dimensional incompressible flow over a stationary flat plate. The problem contains a developing near-wall boundary layer with a strong velocity gradient, while the outer-flow region remains comparatively smooth. It is therefore suitable for examining whether the wavelet indicator can direct refinement toward the wall region without uniformly refining the entire computational domain.

The Reynolds number based on the plate length is

$$Re_L = \frac{\rho U_\infty L}{\mu} = \frac{U_\infty L}{\nu}, \tag{74}$$

where U_∞ is the free-stream velocity, L is the plate length, ρ is the fluid density, μ is the dynamic viscosity, and $\nu = \mu/\rho$ is the kinematic viscosity.

The present benchmark uses

$$Re_L = 1000. \tag{75}$$

At this Reynolds number, the flow is treated as laminar. No turbulence model is employed. The principal physical, numerical, and adaptive parameters are summarized in Table 5.

Table 5. Physical and numerical parameters of the flat-plate benchmark.

Parameter	**Symbol**	**Value**
Reynolds number	Re_L	1000
Analyzed wavelet field	—	Streamwise velocity
Wavelet transform	—	Two-dimensional SWT
Wavelet family	—	db4
Decomposition levels	J	2
Marking fraction	p	20%
Adaptive cycles	—	3
Initial coarse elements	—	256
Final adapted elements	—	4096
Uniform-fine elements	—	16,384

Figure 9 illustrates the computational domain, coordinate system, flat-plate location, and boundary conditions used for the two-dimensional laminar-flow benchmark at $Re_L = 1000$.

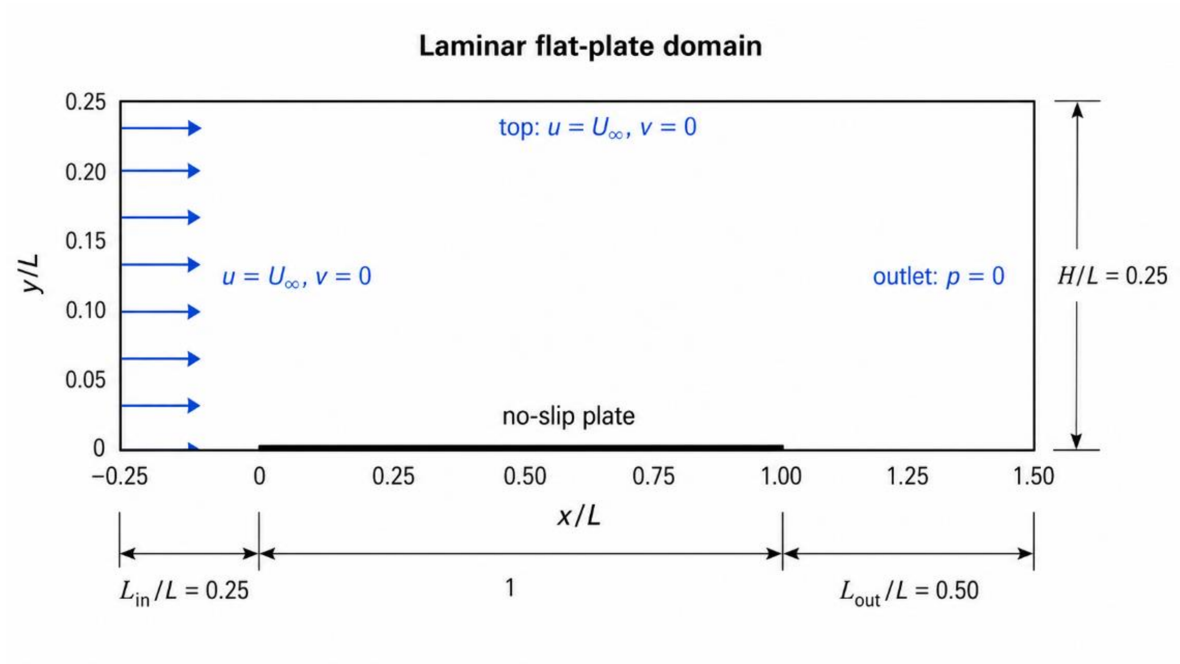

Figure 9. Computational domain and boundary conditions for the two-dimensional laminar flat-plate problem at $Re_L = 1000$. The lower boundary contains the no-slip plate, while the inlet and upper boundary impose the free-stream velocity.

The inlet velocity is prescribed as

$$u = \begin{bmatrix} U_\infty \\ 0 \end{bmatrix}. \tag{76}$$

The no-slip and no-penetration conditions on the plate are

$$u = 0,\ v = 0. \tag{77}$$

The upper boundary represents the undisturbed free stream:

$$u = U_\infty,\ v = 0. \tag{78}$$

At the outlet, the reference pressure is prescribed together with a zero normal velocity gradient:

$$p = 0,\ \frac{\partial u}{\partial n} = 0. \tag{79}$$

4.2.2. Numerical procedure

The incompressible-flow equations are discretized using the mixed finite element formulation described in Section 2.3. The computational domain is partitioned into conforming triangular elements, and the velocity and pressure fields are approximated using the Taylor–Hood P_2/P_1 finite element pair. Accordingly, continuous piecewise-quadratic interpolation is employed for both velocity components, whereas continuous piecewise-linear interpolation is used for pressure. This velocity–pressure pair satisfies the discrete inf–sup stability condition on the conforming meshes considered; therefore, no additional pressure-stabilization term is introduced.

The nonlinear convective term is treated using Picard iteration. At each nonlinear iteration, the convection velocity is evaluated from the preceding iterate, and the resulting linearized mixed velocity–pressure system is solved using a direct sparse solver. The solution on each mesh is considered converged when both the relative change in the discrete velocity field and the relative changes in the monitored skin-friction and drag coefficients are smaller than 10^{-8}. A maximum of 50 nonlinear iterations is permitted. Following mesh refinement, the velocity and pressure fields from the preceding adaptive cycle are interpolated onto the new mesh and used as the initial approximation for the renewed flow solution. The streamwise velocity component

$$g_h^{(m)}(x, y) = u_h^{(m)}(x, y) \tag{80}$$

is transferred to the Cartesian sampling grid and analyzed using the two-dimensional, two-level db4 SWT. The corresponding horizontal, vertical, and diagonal details are combined using Eq (39), and the element-level indicator is computed from Eq (43).

The largest indicator values occur within the developing boundary layer and near the leading-edge region, where the streamwise velocity varies rapidly in the wall-normal direction. At each adaptive cycle, the elements associated with the highest 20% of the normalized indicators are marked for refinement. Additional neighboring elements are refined where required to preserve mesh conformity. The velocity and pressure approximation spaces, together with the diffusion, convection, pressure-coupling, and continuity operators, are then reconstructed on the updated mesh before the nonlinear system is solved again.

Figure 10 presents the initial finite element mesh together with the corresponding streamwise-velocity distribution used as the starting solution for the flat-plate adaptation.

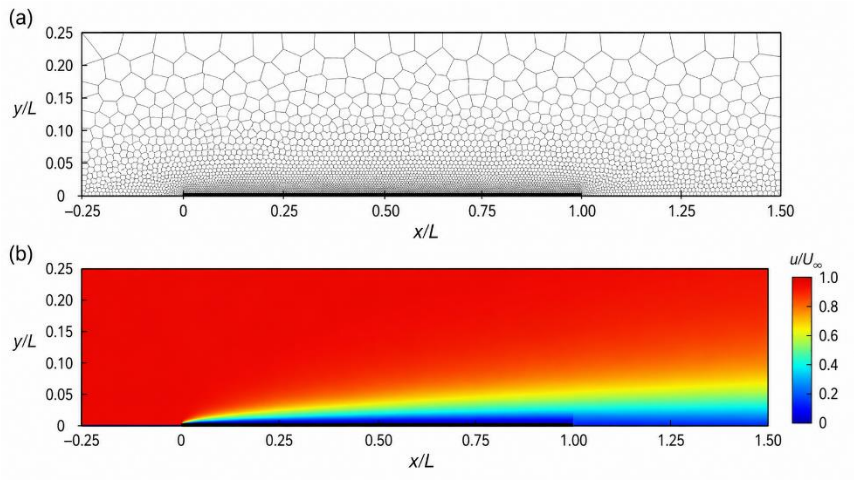

Figure 10. Initial finite element mesh and streamwise-velocity distribution for the flat-plate calculation.

Before adaptive refinement is applied, the sampled streamwise-velocity field is analyzed using a two-level db4 stationary wavelet transform, and the resulting combined detail magnitude—shown in Figure 11—identifies the regions of strongest local variation near the leading edge and within the developing near-wall layer.

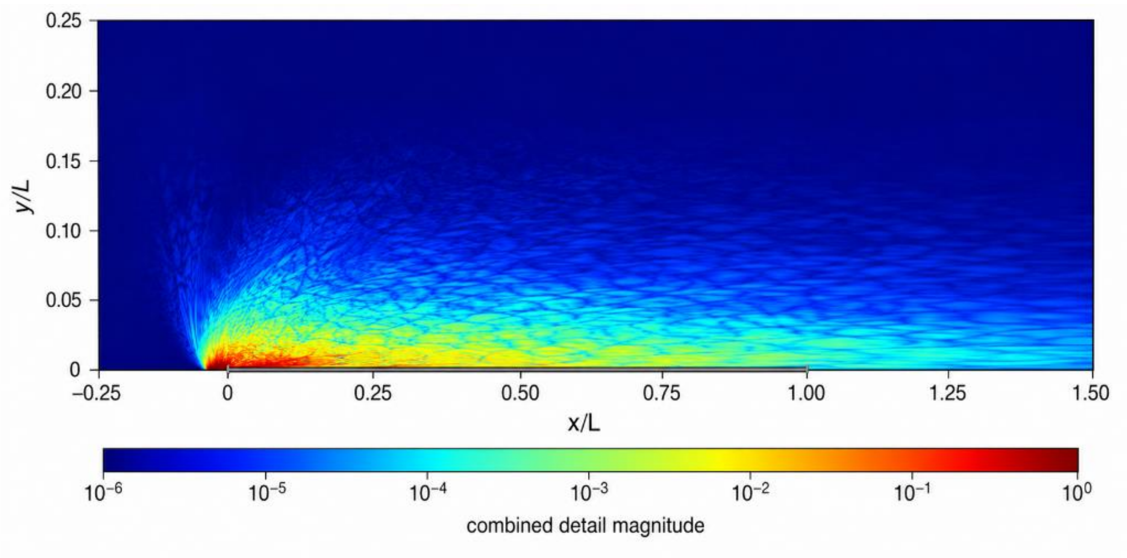

Figure 11. Combined two-level db4 stationary-wavelet detail magnitude obtained from the normalized streamwise-velocity field. The displayed region corresponds to the leading-edge and near-wall portion of the computational domain; coordinates are normalized by the plate length.

4.2.3. Mesh adaptation

The final adapted mesh contains 4096 elements, compared with 16,384 elements in the uniformly refined model. The adapted mesh places most of its additional resolution inside the developing boundary layer, while the outer-flow region remains relatively coarse.

The mesh sizes used in the comparison are summarized in Table 6.

Table 6. Flat-plate mesh sizes and relative problem-size reduction**.**

Mesh	Elements	Relative size
Initial coarse	256	0.0156
Wavelet adapted	4096	0.2500
Uniform fine	16,384	1.0000

The element-count reduction relative to the uniform-fine mesh is

$$R_{\text{el,flow}} = 100\left(1 - \frac{4096}{16\,384}\right) = 75\%. \tag{81}$$

The effect of the wavelet-based refinement strategy on the fluid discretization is illustrated in Figure 12, which compares the final adapted mesh with a uniformly refined mesh and highlights the concentration of elements in the near-wall boundary-layer region.

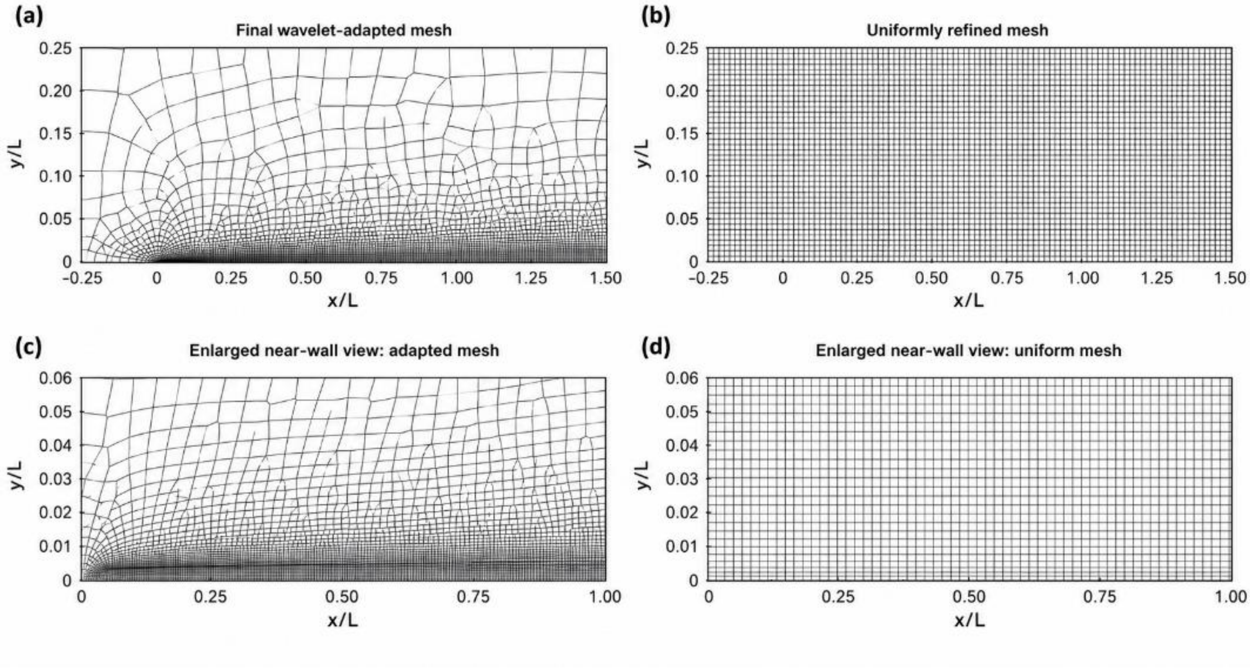

Figure 12. Final wavelet-adapted and uniformly refined flat-plate meshes. Enlarged near-wall views show that the adaptive procedure concentrates elements within the boundary layer.

4.2.4. Wall-shear and drag quantities

The local Reynolds number is

$$Re_x = \frac{\rho U_\infty x}{\mu} = \frac{U_\infty x}{\nu}. \tag{82}$$

The wall shear stress is calculated from the streamwise velocity gradient:

$$\tau_w(x) = \mu \frac{\partial u}{\partial y}\bigg|_{y=0}. \tag{83}$$

The local skin-friction coefficient is

$$C_f(x) = \frac{\tau_w(x)}{\frac{1}{2}\rho U_\infty^2}. \tag{84}$$

For a laminar zero-pressure-gradient boundary layer, the local correlation is

$$C_{f,\mathrm{lam}}(x) = \frac{0.664}{\sqrt{Re_x}}. \tag{85}$$

At the plate end,

$$C_{f,\mathrm{lam}}(L) = \frac{0.664}{\sqrt{Re_L}} = 0.0210. \tag{86}$$

The integrated drag coefficient is defined as

$$C_D = \frac{1}{L}\int_0^L C_f\,(x)\,dx. \tag{87}$$

The corresponding laminar correlation is

$$C_{D,\mathrm{lam}} = \frac{1.328}{\sqrt{Re_L}} = 0.0420. \tag{88}$$

The relative errors in the numerical wall quantities are defined by

$$e_{C_f} = 100\,\frac{|C_{f,h}(L) - C_{f,\mathrm{lam}}(L)|}{C_{f,\mathrm{lam}}(L)}, \tag{89}$$

and

$$e_{C_D} = 100\,\frac{|C_{D,h} - C_{D,\mathrm{lam}}|}{C_{D,\mathrm{lam}}}. \tag{90}$$

4.2.5. Flow results

The numerical wall quantities obtained using the coarse, adapted, and uniform-fine meshes are reported in Table 7.

The coarse mesh underpredicts both the local skin-friction coefficient and the integrated drag coefficient. Its errors are approximately 20%, indicating insufficient near-wall resolution.

Table 7. Flat-plate skin-friction, drag, and computational results.

Mesh	**Elements**	$C_f(L)$	C_f**error (%)**	C_D	C_D**error (%)**	**Time to steady solution (s)**
Initial coarse	256	0.0168	20.0	0.0340	19.0	—
Wavelet adapted	4096	0.0202	3.8	0.0411	2.1	68
Uniform fine	16,384	0.0208	1.0	0.0417	0.7	162
Laminar correlation	—	0.0210	—	0.0420	—	—

The adapted mesh predicts

$$C_f(L) = 0.0202,\ C_D = 0.0411. \tag{91}$$

The corresponding differences from the laminar correlations are approximately 3.8% and 2.1%. The uniform-fine mesh provides slightly smaller errors, but both adapted quantities remain within the selected 5% engineering-accuracy range.

Figure 13 compares the normalized streamwise-velocity contours obtained using the wavelet-adapted and uniform-fine meshes under identical contour levels.

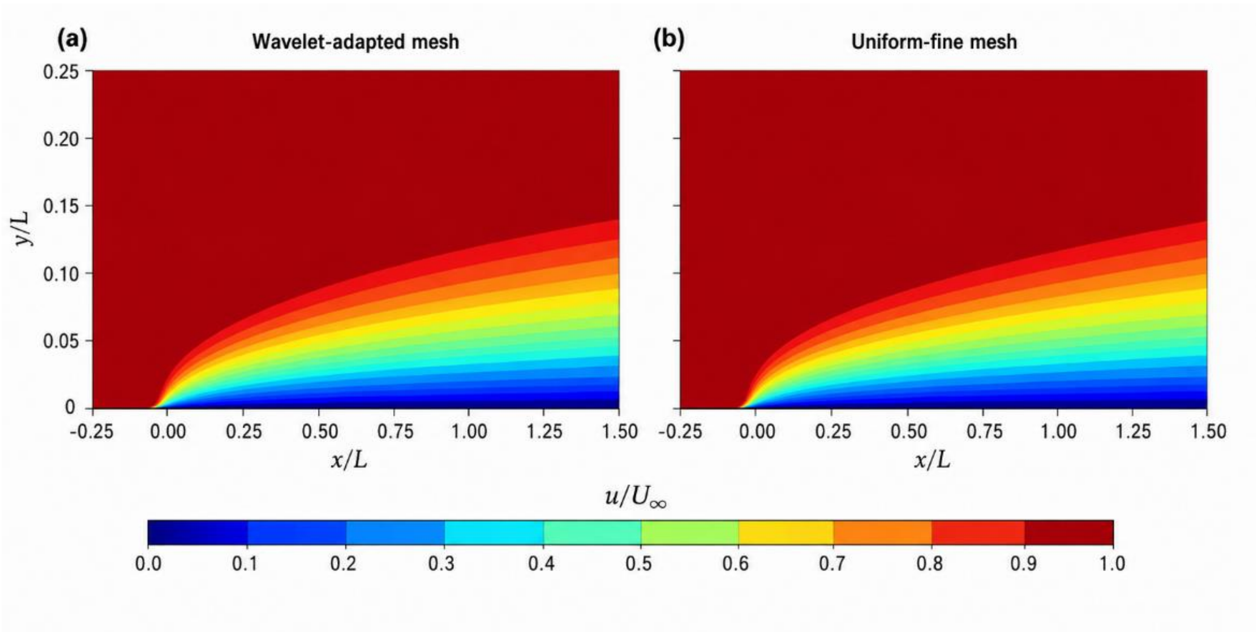

Figure 13. Streamwise-velocity contours obtained using the wavelet-adapted and uniform-fine meshes. Identical contour levels are used for direct comparison.

Figure 14 compares the normalized streamwise-velocity profiles predicted by the wavelet-adapted and uniform-fine meshes at four selected streamwise locations along the flat plate.

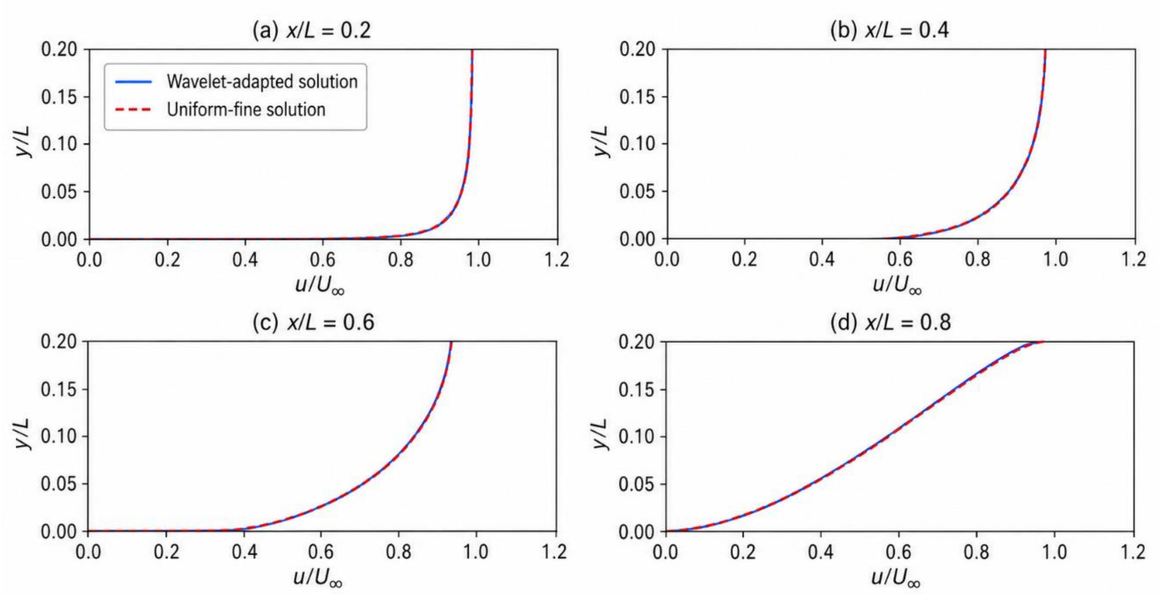

Figure 14. Normalized streamwise-velocity profiles at selected streamwise positions. The adapted and uniform-fine solutions are compared using the same spatial coordinates and velocity normalization.

To evaluate wall-shear prediction and the effect of mesh refinement, Figure 15 compares the local skin-friction coefficient along the flat plate for the initial, wavelet-adapted, and uniform-fine meshes with the classical laminar correlation.

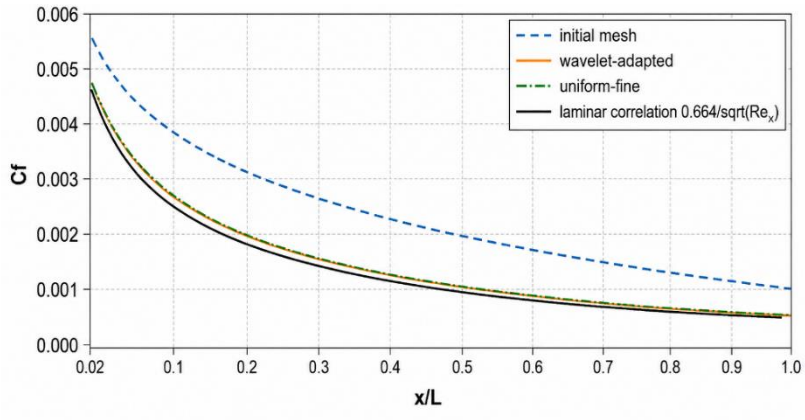

Figure 15. Local skin-friction coefficient along the flat plate for the initial, wavelet-adapted, and uniform-fine meshes, together with the laminar correlation $C_f(x) = 0.664/\sqrt{Re_x}$.

The skin-friction curve should begin downstream of the leading edge because Eq (85) is singular at $x = 0$.

4.2.6. Computational efficiency

The reported time required to reach the steady solution decreases from 162 s for the uniform-fine mesh to 68 s for the complete adapted calculation. The corresponding reduction is

$$R_{t,\mathrm{flow}} = 100\left(1 - \frac{68}{162}\right) = 58.0\%. \tag{92}$$

The runtime ratio is

$$S_{\mathrm{flow}} = \frac{162}{68} = 2.38. \tag{93}$$

The reduction in computational time is smaller than the element-count reduction because the adaptive procedure introduces additional operations associated with field sampling, wavelet transformation, coefficient mapping, mesh reconstruction, solution transfer, and repeated finite element solutions.

The field-level difference from a reference solution may be evaluated using

$$e_u = \frac{\|u_h - u_{\mathrm{ref}}\|_{L^2(\Omega_f)}}{\|u_{\mathrm{ref}}\|_{L^2(\Omega_f)}}. \tag{94}$$

If a pointwise root-mean-square measure is used instead, it is defined as

$$\mathrm{RMSE}_u = \left[\frac{1}{N_s}\sum_{q=1}^{N_s}\left(u_{h,q} - u_{\mathrm{ref},q}\right)^2\right]^{1/2}, \tag{95}$$

where N_s is the number of comparison points. The 16,384-element uniform-fine solution is used as the reference field. The wavelet-adapted and reference solutions are interpolated onto the same comparison grid before evaluating the pointwise absolute difference and the field-error measures.

Figure 16 shows the spatial distribution of the absolute difference between the wavelet-adapted and reference streamwise-velocity fields, with the largest discrepancies concentrated near the leading edge and within the developing boundary layer.

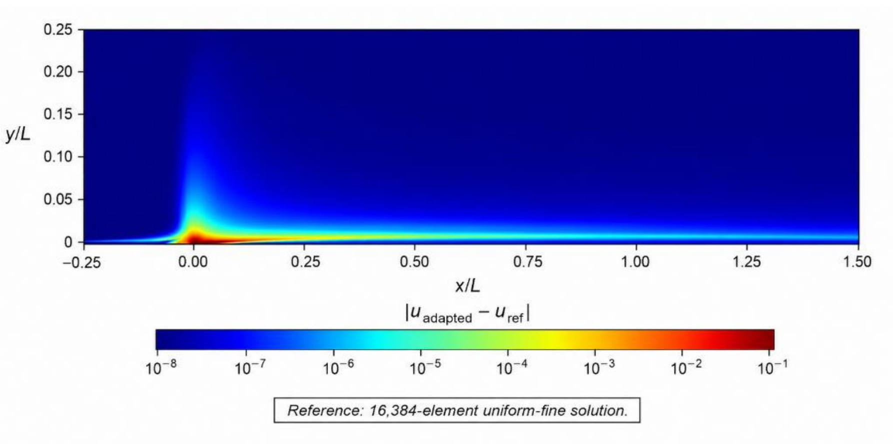

Figure 16. Absolute difference between the wavelet-adapted and reference streamwise-velocity fields.

4.3. Summary of the two benchmarks

The principal accuracy and computational results are summarized in Table 8.

Table 8. Summary of the wavelet-adapted and uniform-fine results.

Benchmark	Quantity	Wavelet adapted	Uniform fine	Adaptive reduction
Beam	Elements	60	160	62.5%
Beam	Active DOFs	120	320	62.5%
Beam	Maximum error in first three frequencies	3.8%	3.5%	—
Beam	Modal-solution time	1.90 s	4.40 s	56.8%
Flat plate	Elements	4096	16,384	75.0%
Flat plate	$C_f(L)$ error	3.8%	1.0%	—
Flat plate	C_D error	2.1%	0.7%	—
Flat plate	Time to steady solution	68 s	162 s	58.0%

The uniformly refined models remain slightly more accurate in the reported quantities. The benefit of the adapted models is that they satisfy the selected accuracy ranges using substantially fewer elements and lower reported computational times. The results, therefore, demonstrate an improved accuracy–cost balance rather than universal superiority in numerical accuracy.

5. Results and discussion

The two numerical applications examine the wavelet-guided adaptive procedure under different physical and numerical conditions. The beam benchmark evaluates modal and frequency-response accuracy in a one-dimensional structural model, whereas the flat-plate benchmark examines the resolution of a two-dimensional near-wall velocity gradient. The results are discussed in terms of matched accuracy, computational efficiency, indicator localization, relation to established adaptive strategies, parameter dependence, and computational overhead.

5.1. Matched-accuracy criteria

A meaningful efficiency comparison requires the adapted and uniformly refined solutions to satisfy comparable accuracy requirements. In this study, matched accuracy does not imply identical numerical values. It means that both discretizations satisfy the same prescribed engineering-accuracy range.

For the beam benchmark, the accuracy criterion is based on the maximum relative error among the first three natural frequencies:

$$e_{f,\max} = \max_{n=1,2,3}\left[100\,\frac{\left|f_{n,h} - f_n^{\text{exact}}\right|}{f_n^{\text{exact}}}\right]. \tag{96}$$

The selected modal-accuracy requirement is

$$e_{f,\max} \leq 4\%. \tag{97}$$

For the flat-plate benchmark, the accuracy criteria are based on the end-of-plate skin-friction coefficient and the integrated drag coefficient:

$$e_{C_f} = 100\frac{\left|C_{f,h}(L) - C_{f,\mathrm{lam}}(L)\right|}{C_{f,\mathrm{lam}}(L)}, \tag{98}$$

and

$$e_{C_D} = 100\frac{\left|C_{D,h} - C_{D,\mathrm{lam}}\right|}{C_{D,\mathrm{lam}}}. \tag{99}$$

The corresponding requirements are

$$e_{C_f} \leq 5\%, \qquad e_{C_D} \leq 5\%. \tag{100}$$

The adapted and uniformly refined solutions are therefore compared after both satisfy the relevant benchmark-specific accuracy conditions.

5.2. Accuracy and computational efficiency

5.2.1. Structural benchmark

The initial 12-element beam mesh produces relative errors of 7.3%, 14.9%, and 28.1% in the first three natural frequencies. The progressive increase in error with mode number is expected because the higher modes contain shorter spatial wavelengths and greater modal curvature, which require finer spatial resolution.

After three adaptive cycles, the 60-element wavelet-adapted mesh reduces the errors to 1.2%, 2.5%, and 3.8%. The 160-element uniformly refined mesh gives corresponding errors of 1.0%, 2.2%, and 3.5%. Both meshes, therefore, satisfy the 4% modal-accuracy requirement defined in Eq (97).

The uniform-fine result remains slightly more accurate, particularly for the second and third frequencies. The main advantage of the adapted model is therefore not higher absolute accuracy but the ability to reach the selected accuracy range using fewer active degrees of freedom.

The reduction in active degrees of freedom is

$$R_{\mathrm{dof}} = 100\left(1 - \frac{N_{\mathrm{dof}}^{\mathrm{adapt}}}{N_{\mathrm{dof}}^{\mathrm{uniform}}}\right) = 100\left(1 - \frac{120}{320}\right) = 62.5\%. \tag{101}$$

The reported modal-solution time decreases from 4.40 to 1.90 s, corresponding to

$$R_{t,\mathrm{beam}} = 100\left(1 - \frac{1.90}{4.40}\right) = 56.8\%. \tag{102}$$

The adapted model also reproduces the first two resonance locations at approximately 23.4 Hz and 93.1 Hz. Their deviations from the corresponding analytical frequencies are approximately 0.55% and 1.07%, respectively. The agreement between the eigenvalue and frequency-response results confirms that the adapted discretization provides adequate resolution for the principal dynamic characteristics considered in this study.

5.2.2. Fluid benchmark

The initial 256-element flat-plate mesh underpredicts both wall quantities. Its end-of-plate skin-friction coefficient differs from the laminar correlation by approximately 20%, while the integrated drag error is approximately 19%. These errors indicate that the coarse mesh does not provide sufficient near-wall resolution.

The 4096-element wavelet-adapted mesh predicts

$$C_f(L) = 0.0202, \qquad C_D = 0.0411,$$

with relative differences of approximately 3.8% and 2.1% from the corresponding laminar correlations. The 16,384-element uniform-fine mesh gives slightly smaller errors of approximately 1.0% and 0.7%.

Both refined solutions satisfy the 5% requirements defined in Equation (100). As in the structural benchmark, the uniformly refined mesh is more accurate in the reported quantities, whereas the adapted mesh reaches the prescribed accuracy range with a substantially smaller global problem size.

The reduction in the number of elements is

$$R_{\mathrm{el,flow}} = 100\left(1 - \frac{N_{\mathrm{el}}^{\mathrm{adapt}}}{N_{\mathrm{el}}^{\mathrm{uniform}}}\right) = 100\left(1 - \frac{4096}{16\,384}\right) = 75.0\%. \quad (103)$$

The reported time to reach the steady solution decreases from 162 to 68 s:

$$R_{t,\mathrm{flow}} = 100\left(1 - \frac{68}{162}\right) = 58.0\%. \quad (104)$$

The velocity contours and profiles show close agreement between the adapted and uniform-fine solutions over most of the fluid domain. The largest differences occur near the leading edge and inside the developing boundary layer, where the velocity gradient is strongest and where wall-derived quantities are most sensitive to the discretization.

The principal results from both applications are summarized in Table 9.

Table 9. Consolidated comparison of the wavelet-adapted and uniform-fine solutions.

Benchmark	**Quantity**	**Wavelet adapted**	**Uniform fine**	**Reduction or difference**
Beam	Elements	60	160	62.5% reduction
Beam	Active DOFs	120	320	62.5% reduction
Beam	Maximum error in f_1–f_3	3.8%	3.5%	0.3 percentage points
Beam	Modal-solution time	1.90 s	4.40 s	56.8% reduction
Beam	Runtime ratio	2.32 × faster	Reference	—
Flat plate	Elements	4096	16,384	75.0% reduction
Flat plate	$C_f(L)$ error	3.8%	1.0%	2.8 percentage points
Flat plate	C_D error	2.1%	0.7%	1.4 percentage points
Flat plate	Time to steady solution	68 s	162 s	58.0% reduction
Flat plate	Runtime ratio	2.38 × faster	Reference	—

The values in Table 9 show that the adapted discretizations provide an improved accuracy–cost balance. The results do not indicate that adaptation produces smaller errors than uniform refinement at the same final refinement level. Instead, they show that the selected engineering-accuracy ranges can be reached with fewer elements and lower reported computational time.

The relative reductions in global problem size and computational time are compared in Figure 17 after normalization by the corresponding uniform-fine values.

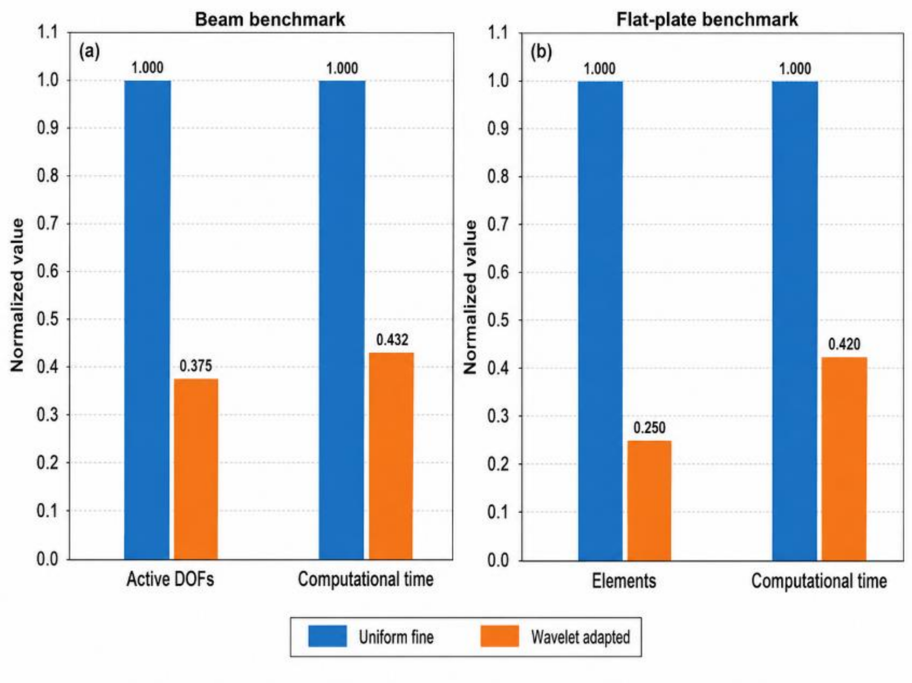

Figure 17. Normalized problem size and computational time for the wavelet-adapted and uniform-fine models. Each value is normalized by the corresponding uniform-fine result; lower adapted values indicate reduced computational requirements at the selected matched-accuracy criteria.

5.3. Spatial behavior of the wavelet indicator

The two benchmarks demonstrate that the wavelet indicator responds to localized spatial variations in fields with different physical meanings.

In the beam problem, the displacement details become significant in regions where the transverse field changes rapidly and where the excitation influences the local spatial response. Refinement in these regions improves the higher modal frequencies, which are more sensitive to local mesh resolution than the first mode. In the flat-plate problem, the largest detail magnitudes occur close to the leading edge and inside the developing boundary layer. These regions are characterized by a strong wall-normal variation of the streamwise velocity. The adapted mesh consequently concentrates elements near the plate while retaining a coarser discretization in the outer-flow region.

This behavior illustrates an important practical feature of the approach: the same general coefficient-aggregation and marking procedure can be applied to different physical fields. However, a large wavelet coefficient does not uniquely identify discretization error. It may also result from a genuine physical gradient, a singularity, interpolation to the sampling grid, numerical oscillation, or the boundary treatment used by the transform. For this reason, the indicator should be interpreted together with the convergence of physically relevant output quantities. In the present study, these quantities are the modal frequencies and resonance locations for the beam and the skin-friction and drag coefficients for the flat plate.

5.4. Relation to conventional adaptive indicators

Established adaptive finite element procedures commonly employ residual-, recovery-, hierarchical-, or goal-oriented indicators [5,34,35]. These approaches differ from the present wavelet method in the type of information used to guide refinement. Recent applications also illustrate the diversity of refinement criteria: element subdivision–based estimators have been used for vibration eigensolutions in cracked elasticity [10], whereas prescribed refinement patches and coarse–fine interface treatments have been employed in multiscale plasma simulations [11]. These approaches reinforce the need to select the refinement mechanism according to the governing formulation, target quantity, and available error-control requirements.

5.4.1 Residual-based indicators

A residual-based indicator generally combines the element residual with inter-element jump terms. A representative form is

$$\eta_{e,\mathrm{res}}^2 = h_e^2 \|R_e\|_{L^2(e)}^2 + \frac{1}{2} \sum_{\gamma \subset \partial e} h_\gamma \, \|J_\gamma\|_{L^2(\gamma)}^2, \tag{105}$$

where R_e is the residual of the governing equation within element e, J_γ denotes a flux or traction jump across edge γ, and h_e and h_γ are characteristic element and edge dimensions.

Residual estimators have a direct connection with the governing equation and can provide reliability and efficiency results under appropriate assumptions. Their construction, however, depends on the differential operator, boundary conditions, finite element space, and selected error norm.

5.4.2. Recovery-based indicators

Recovery-based methods compare a finite element quantity with a reconstructed field having improved continuity or smoothness. In structural mechanics, a representative stress-recovery indicator is

$$\eta_{e,\mathrm{rec}}^2 = \int_e (\boldsymbol{\sigma}^* - \boldsymbol{\sigma}_h)^T \, \mathbf{D}^{-1} (\boldsymbol{\sigma}^* - \boldsymbol{\sigma}_h) \, d\Omega, \tag{106}$$

where $\boldsymbol{\sigma}_h$ is the finite element stress, $\boldsymbol{\sigma}^*$ is the recovered stress, and $\mathbf{D}$ is the constitutive matrix.

Recovery-based approaches are effective when the recovered field is sufficiently accurate, but they require an additional reconstruction procedure and are usually formulated for a specific physical quantity [8].

5.4.3. Position of the wavelet indicator

The proposed wavelet indicator is field-based rather than residual-based. Its practical strengths are:

- simultaneous localization in position and scale;
- a common analysis procedure for different physical fields;
- sensitivity to localized and multiscale variations;
- no requirement to derive an equation-specific residual expression.

Its principal limitations are:

- absence of a general guaranteed error bound;
- dependence on the selected field and wavelet parameters;
- sensitivity to boundary treatment;
- the need to transfer an irregular finite element field to an ordered sampling grid.

The wavelet approach is therefore regarded as a complementary refinement mechanism. Residual- and recovery-based estimators remain preferable when mathematically justified error control, equilibrium information, or proven reliability and efficiency properties are required.

5.5. Influence of wavelet and marking parameters

The adaptive mesh produced by the method depends on the wavelet family, decomposition level, sampling resolution, boundary-extension procedure, and marking fraction.

The db4 wavelet was selected because it provides compact support together with sufficient smoothness for the displacement and velocity fields considered. Two decomposition levels were used to combine fine and intermediate spatial information without spreading the indicator excessively over the domain. A lower-order wavelet has shorter support and may respond more strongly to abrupt local changes, but it can also be more sensitive to numerical noise. A higher-order wavelet provides greater smoothness and additional vanishing moments, although its larger support can reduce spatial selectivity near localized features and boundaries.

The decomposition level also affects localization. A low level primarily identifies fine-scale content, whereas higher levels include progressively broader spatial variations. Excessive decomposition may cause the indicator to extend beyond the region that requires refinement. The fixed marking fraction determines the rate of mesh growth. A small value of p restricts the number of refined elements but may require additional cycles to capture all relevant regions. A large value increases the problem size more rapidly and may approach uniform refinement. The value $p = 20\%$ was used consistently in both applications to provide controlled mesh growth while retaining local selectivity.

The selected wavelet and marking parameters are benchmark settings rather than universal optimum values. Their suitability should be evaluated for problems with substantially different regularity, geometry, or physical scales.

5.6. Computational overhead

The total computational cost of the adaptive procedure can be expressed as

$$T_{\text{adapt}} = T_{\text{FE}} + T_{\text{sample}} + T_{\text{WT}} + T_{\text{map}} + T_{\text{mesh}} + T_{\text{transfer}}, \tag{107}$$

where:

- T_{FE} is the finite element assembly and solution time.
- T_{sample} is the field-sampling time.
- T_{WT} is the wavelet-transform time.
- T_{map} is the coefficient-to-element mapping time
- T_{mesh} is the marking and mesh-reconstruction time.
- T_{transfer} is the solution-transfer time.

The relative adaptive overhead is

$$r_{\text{overhead}} = 100\frac{T_{\text{sample}} + T_{\text{WT}} + T_{\text{map}} + T_{\text{mesh}} + T_{\text{transfer}}}{T_{\text{adapt}}}. \tag{108}$$

The wavelet transform itself has approximately linear complexity with respect to the number of samples for the one-dimensional DWT and approximately $O(JN_G)$ complexity for a J-level SWT. In larger finite element models, assembly and algebraic solutions generally dominate the total runtime. In smaller calculations, sampling, mapping, and mesh reconstruction can represent a more noticeable fraction of the total cost.

The reported timing reductions of 56.8% for the beam and 58.0% for the flat plate result from the smaller adapted systems, despite the additional adaptive operations. These timing values should be interpreted within the computational environment used for the study because they depend on the hardware, software implementation, solver settings, and stopping criteria.

5.7. Practical applicability

The results indicate that wavelet-guided refinement is most useful when the quantity of interest is influenced by localized spatial behavior. Examples include structural curvature, stress concentrations, boundary layers, localized transport fronts, and strongly varying acoustic or vibration fields.

The analyzed field must be selected according to the intended output. Displacement-based refinement may be appropriate for modal displacement accuracy, whereas curvature or stress may be more suitable when local bending stress is the principal quantity of interest. In incompressible flow, streamwise velocity emphasizes boundary-layer development, while pressure or vorticity would produce different refinement patterns. The method does not replace the requirements of the underlying finite element formulation. Stable mixed spaces or appropriate stabilization remain necessary for incompressible flow, and mesh refinement does not remove shear locking, volumetric locking, or other element-formulation deficiencies. This distinction is consistent with recent plate and shell finite element studies showing that specialized interpolation, projected-shear techniques, or enriched formulations may be required to suppress shear locking and maintain accurate behavior across thin and thick structural regimes [21–24].

The present results support the use of wavelet analysis as a practical localization tool within a conventional finite element workflow. The principal contribution is the improved distribution of computational resolution rather than a universal increase in numerical accuracy.

5.8. Overall assessment

The beam and flat-plate applications demonstrate that the wavelet-enhanced adaptive procedure can direct refinement toward regions containing strong localized variations while limiting unnecessary refinement elsewhere. For the beam, the adapted model satisfies the 4% modal-accuracy criterion using 62.5% fewer active degrees of freedom than the uniformly refined model. For the flat plate, the adapted mesh satisfies the 5% skin-friction and drag criteria using 75% fewer elements.

The reported computational-time reductions are approximately 56.8% and 58.0%, respectively. These gains are accompanied by slightly larger errors than those of the uniform-fine solutions, but the adapted results remain within the selected accuracy ranges. The numerical evidence, therefore, supports the wavelet indicator as a useful complementary mechanism for improving the accuracy–cost balance of finite element calculations involving localized spatial features.

6. Conclusions

This study developed a wavelet-enhanced adaptive finite element procedure for structural and fluid-dynamics applications. The conventional finite element formulation was retained, while multiresolution wavelet analysis was introduced to identify regions containing strong localized variations. At each adaptive cycle, the selected finite element field was sampled, decomposed into wavelet-detail components, converted into element-level indicators, and used to guide local refinement before reassembly and solution on the updated mesh. The procedure was evaluated using a one-dimensional simply supported Euler–Bernoulli beam and a two-dimensional laminar flat-plate boundary-layer problem at $Re_L = 1000$. These benchmarks were selected to assess the method for two distinct types of localized behavior: modal variation in a structural displacement field and a strong near-wall gradient in a fluid-velocity field.

For the beam problem, the wavelet-adapted mesh reproduced the first three analytical natural frequencies with a maximum relative error of 3.8%, compared with 3.5% for the uniformly refined model. The adapted discretization used 120 active degrees of freedom instead of 320, corresponding to a reduction of 62.5%. The reported modal-solution time decreased from 4.40 to 1.90 s, while the first two resonance locations remained close to the analytical values. For the flat-plate problem, the adaptive procedure concentrated refinement near the leading edge and within the developing boundary layer while maintaining a coarser outer-flow region. The adapted mesh contained 4096 elements, compared with 16,384 elements for the uniform-fine model, giving a 75% reduction in element count. The adapted solution predicted the end-of-plate skin-friction and integrated drag coefficients with relative differences of approximately 3.8% and 2.1% from the corresponding laminar correlations. The reported time to reach the steady solution decreased from 162 to 68 s.

The results indicate that the main benefit of the proposed method is an improved balance between numerical accuracy and computational cost. The uniformly refined solutions remained slightly more accurate in several reported quantities; therefore, the wavelet-guided procedure should not be interpreted as universally more accurate than uniform refinement. Its advantage is that the selected engineering-accuracy requirements were reached using substantially smaller computational models. The wavelet coefficients used in this study are refinement indicators rather than rigorous a posteriori error estimators. Their effectiveness depends on the analyzed field, wavelet family, decomposition level, sampling resolution, boundary treatment, and marking strategy. Moreover, wavelet-guided refinement does not correct deficiencies in the underlying finite element formulation, such as locking, unstable mixed spaces, or inadequate stabilization.

The proposed approach should therefore be regarded as complementary to residual-, recovery-, and goal-oriented adaptive methods. Future work will focus on direct comparisons with established estimators under identical refinement budgets, adaptive selection of wavelet parameters, conservative transfer between successive meshes, direct treatment of unstructured data, and extension to three-dimensional, nonlinear, transient, and higher-Reynolds-number problems.

Author contributions

For research "Conceptualization, Zeineb Klai, Mohamed Ayari, Atef Gharbi, Omar Kahouli, Fahd

Alhamazani; methodology, all authors; software, all authors; validation, all authors; formal analysis, all authors; investigation, all authors; resources, Zeineb Klai and Nasser Albalwi; data curation, all authors; writing—original draft preparation, all authors; writing—review and editing, all authors; visualization, all authors; supervision, Zeineb Klai and Mohamed Ayari; project administration, Sulaiman Almohaimeed; funding acquisition, Sulaiman Almohaimeed. All authors have read and agreed to the published version of the manuscript.”.

Use of Generative-AI tools declaration

The authors used ChatGPT (OpenAI) solely for English language and grammar editing during manuscript preparation. The authors reviewed and verified the final manuscript and are fully responsible for its accuracy, originality, and integrity.

Acknowledgments

The authors extend their appreciation to the Deanship of Scientific Research at Northern Border University, Arar, KSA for funding this research work through the project number NBU-FPEJ-2026 2942-03.

Conflict of interest

The authors declare no conflicts of interest. The funders had no role in the design of the study; in the collection, analyses, or interpretation of data; in the writing of the manuscript; or in the decision to publish the result.

References

1. H. Temimi, S. Adjerid, M. Ayari, Implementation of the discontinuous Galerkin method on a multi-story seismically excited building model, *Eng. Lett.,* **18** (2010), Article EL_18_1_03.
2. Z. X. Sun, G. Y. Jin, T. G. Ye, K. Y. Song, Y. K. Chen, A three-dimensional B-spline wavelet finite element method for structural vibration analysis, *J. Vib. Control*, **29** (2023), 5683–5697. https://doi.org/10.1177/10775463221138938
3. Z. Sun, G. Jin, T. Ye, Y. Chen, K. Song, Interior three-dimensional acoustic modeling and modal analysis using wavelet-based finite-element approach, *J. Acoust. Soc. Am.*, **156** (2024), 1252–1268. https://doi.org/10.1121/10.0028311
4. A. G. Prinn, A review of finite element methods for room acoustics, *Acoustics*, **5** (2023), 367–395. https://doi.org/10.3390/acoustics5020022
5. A. Bonito, C. Canuto, R. H. Nochetto, A. Veeser, Adaptive finite element methods, *Acta Numer.*, **33** (2024), 163–485. https://doi.org/10.1017/S0962492924000011
6. H. Li, T. Yamada, P. Jolivet, K. Furuta, T. Kondoh, K. Izui, et al., Full-scale 3D structural topology optimization using adaptive mesh refinement based on the level-set method, *Finite Elem. Anal. Des.*, **194** (2021), 103561. https://doi.org/10.1016/j.finel.2021.103561
7. M. V. Pham, M. N. Nguyen, T. Q. Bui, An adaptive mesh refinement algorithm for crack propagation with an enhanced thermal–mechanical local damage model, *Finite Elem. Anal. Des.*, **243** (2025), 104278. https://doi.org/10.1016/j.finel.2024.104278

8. T. Tian, C. Chen, L. He, H. Wei, Adaptive finite element method for phase field fracture models based on recovery error estimates, *J. Comput. Appl. Math.*, **472** (2026), 116732. https://doi.org/10.1016/j.cam.2025.116732
9. C. Carstensen, B. Gräßle, Rate-optimal higher-order adaptive conforming FEM for biharmonic eigenvalue problems on polygonal domains, *Comput. Methods Appl. Mech. Eng.*, **425** (2024), 116931. https://doi.org/10.1016/j.cma.2024.116931
10. Y. Wang, Y. Cui, J. Wang, Y. Ju, An -version adaptive finite element scheme for eigensolutions of free vibration of three-dimensional cracked elasticity utilizing element subdivision-based error estimator, *J. Intell. Constr.*, **3** (2025), 9180078. https://doi.org/10.26599/JIC.2025.9180078
11. R. Jambunathan, H. Jones, L. Corrales, H. Klion, M. E. Rowan, A. Myers, et al., Application of mesh refinement to relativistic magnetic reconnection, *Phys. Plasmas*, **32** (2025), 013905. https://doi.org/10.1063/5.0233583
12. C. M. Akujuobi, *Wavelets and Wavelet Transform Systems and Their Applications: A Digital Signal Processing Approach*, Springer International Publishing, 2022. https://doi.org/10.1007/978-3-030-87528-2
13. Z. Klai, M. Ayari, K. Kefi, M. A. Hammami, A. ElKamel, A. Gharbi, et al., Comparative analysis of Fourier transform variants: Performance, applications, and efficiency, *J. Comput. Anal. Appl.*, **33** (2024), 841–852.
14. R. Stevenson, R. van Venetië, J. Westerdiep, A wavelet-in-time, finite element-in-space adaptive method for parabolic evolution equations, *Adv. Comput. Math.*, **48** (2022), Article 17. https://doi.org/10.1007/s10444-022-09930-w
15. S. Kestler, K. Steih, K. Urban, An efficient space-time adaptive wavelet Galerkin method for time-periodic parabolic partial differential equations, *Math. Comput.*, **85** (2016), 1309–1333. https://doi.org/10.1090/mcom/3009
16. R. van Venetië, *Operator Preconditioning and Space-Time Methods for Parabolic Evolution Equations*, Doctoral dissertation, University of Amsterdam, 2021.
17. R. van Venetië, J. Westerdiep, Efficient space-time adaptivity for parabolic evolution equations using wavelets in time and finite elements in space, *Numer. Linear Algebra Appl.*, **30** (2023), e2457. https://doi.org/10.1002/nla.2457
18. S. Fu, E. T. Chung, G. Li, Wavelet-based edge multiscale finite element methods for singularly perturbed convection-diffusion equations, *Multiscale Model. Simul.*, **23** (2025), 431–457. https://doi.org/10.1137/24M1659017
19. Q. Wei, J. Xiang, B-spline wavelet boundary element method for three-dimensional problems, *Acta Mech.*, **232** (2021), 3233–3257. https://doi.org/10.1007/s00707-021-03009-1
20. W. Ding, L. Li, H. Zhong, Y. Li, D. Bao, S. Wei, et al., A semi-analytical wavelet finite element method for wave propagation in rectangular rods, *Wave Motion*, **128** (2024), 103325. https://doi.org/10.1016/j.wavemoti.2024.103325
21. Z. Belabed, M. A. Kenanda, F. Hammadi, H. M. Sedighi, Shear-locking-free finite element formulation for vibrating functionally graded graphene nanocomposites using an enriched quadrilateral plate element, *Eng. Comput.*, **41** (2025), 4393–4415. https://doi.org/10.1007/s00366-025-02210-3
22. S. Widyatmoko, J. L. Batoz, I. Katili, F. Hammadi, A new performing quadrilateral finite element with 24 degrees of freedom valid for thin and thick shell modelling: Formulation aspects and numerical results, *Int. J. Numer. Methods Eng.*, **126** (2025), e70207. https://doi.org/10.1002/nme.70207

23. Z. Belabed, A new application of quadrilateral finite element model incorporating the discrete shear projection technique for free vibration response of CNT reinforced plates, *Int. J. Solids Struct.*, **309** (2025), 113204. https://doi.org/10.1016/j.ijsolstr.2024.113204
24. B. Bendaho, A. Mesbah, Z. Belabed, A new quadrilateral finite element formulation for the free vibration analysis of CNT-reinforced plates with cutouts, *Comput. Mater. Continua*, **85** (2025), 2781–2805. https://doi.org/10.32604/cmc.2025.069709
25. S. Dan, P. Tarafder, S. Ghosh, Adaptive wavelet-enhanced cohesive zone phase-field FE model for crack evolution in piezoelectric composites, *Comput. Methods Appl. Mech. Eng.*, **392** (2022), 114636. https://doi.org/10.1016/j.cma.2022.114636
26. G. Zhang, C. Tang, P. Chen, G. Long, J. Cao, S. Tang, Advancements in phase-field modeling for fracture in nonlinear elastic solids under finite deformations, *Mathematics*, **11** (2023), 3366. https://doi.org/10.3390/math11153366
27. H. K. Wang, X. Zhang, H. Long, S. Yao, P. Zhu, W-FENet: Wavelet-based Fourier-enhanced network model decomposition for multivariate long-term time-series forecasting, *Neural Process. Lett.*, **56** (2024), Article 43. https://doi.org/10.1007/s11063-024-11478-3
28. J. Li, H. Xie, L. Yu, Y. Zhang, Wavelet-enhanced weakly supervised local feature learning for face forgery detection, in *Proceedings of the 30th ACM International Conference on Multimedia*, Association for Computing Machinery, (2022), 1299–1308. https://doi.org/10.1145/3503161.3547832
29. J. Lin, W. Zhou, A wavelet-based denoising method for pipeline dent assessments, *Comput. Struct.*, **303** (2024), 107497. https://doi.org/10.1016/j.compstruc.2024.107497
30. R. R. Craig, Jr., A. J. Kurdila, *Fundamentals of Structural Dynamics*, 2nd ed., John Wiley & Sons, 2006.
31. Y. A. Mishin, O. V. Vasilyev, T. V. Gerya, A wavelet-based adaptive finite element method for the Stokes problems, *Fluids*, **7** (2022), 221. https://doi.org/10.3390/fluids7070221
32. Y. Mehta, A. Nejadmalayeri, J. D. Regele, Computational fluid dynamics using the adaptive wavelet-collocation method, *Fluids*, **6** (2021), 377. https://doi.org/10.3390/fluids6110377
33. M. A. Alkhonaini, E. Gemeay, F. M. Z. Mahmood, M. Ayari, F. A. Alenizi, S. Lee, A new encryption algorithm for image data based on two-way chaotic maps and iterative cellular automata, *Sci. Rep.*, **14** (2024), 16701. https://doi.org/10.1038/s41598-024-64741-x
34. O. C. Zienkiewicz, J. Z. Zhu, A simple error estimator and adaptive procedure for practical engineering analysis, *Int. J. Numer. Methods Eng.*, **24** (1987), 337–357. https://doi.org/10.1002/nme.1620240206
35. R. Verfürth, *A Review of A Posteriori Error Estimation and Adaptive Mesh-Refinement Techniques*, Wiley-Teubner, 1996.
36. R. E. Bird, C. E. Augarde, W. M. Coombs, R. Duddu, S. Giani, P. T. Huynh, et al., An -adaptive discontinuous Galerkin method for phase field fracture, *Comput. Methods Appl. Mech. Eng.*, **416** (2023), 116336. https://doi.org/10.1016/j.cma.2023.116336
37. A. Gupta, U. M. Krishnan, T. K. Mandal, R. Chowdhury, V. P. Nguyen, An adaptive mesh refinement algorithm for phase-field fracture models: Application to brittle, cohesive, and dynamic fracture, *Comput. Methods Appl. Mech. Eng.*, **399** (2022), 115347. https://doi.org/10.1016/j.cma.2022.115347